GAS-PHASE FORMATION RATES OF NITRIC ACID AND ITS ISOMERS UNDER URBAN CONDITIONS

FINAL REPORT
CONTRACT NO. 03-333

PREPARED FOR:

CALIFORNIA AIR RESOURCES BOARD
RESEARCH DIVISION
1001 I STREET
SACRAMENTO, CALIFORNIA 95814

PREPARED BY:

MITCHIO OKUMURA, PRINCIPAL INVESTIGATOR
RESEARCHERS:
ANDREW K. MOLLNER
JULIANE L. FRY
LIN FENG
DIVISION OF CHEMISTRY AND CHEMICAL ENGINEERING
CALIFORNIA INSTITUTE OF TECHNOLOGY
PASADENA, CALIFORNIA 91125

AND

STANLEY P. SANDER, PRINCIPAL INVESTIGATOR
VALLUVADASAN SIVAKUMARAN, RESEARCHER
EARTH AND SPACE SCIENCES DIVISION
NASA JET PROPULSION LABORATORY
CALIFORNIA INSTITUTE OF TECHNOLOGY
PASADENA, CALIFORNIA 91109

NOVEMBER 2005

Disclaimer

The statements and conclusions in this report are those of the Contractor and not necessarily those of the California Air Resources Board. The mention of commercial products, their sources, or their use in connection with material reported herein is not to be construed as actual or implied endorsement of such products.

Acknowledgements

This Report was submitted in fulfillment of Contract No. 03-333, "Gas-Phase Formation Rates of Nitric Acid and its Isomers under Urban Conditions" by the California Institute of Technology and NASA Jet Propulsion Laboratory under the sponsorship of the California Air Resources Board. Supplementary support came from the National Aeronautics and Space Administration (NASA) Upper Atmosphere Research Program. Andrew Mollner was supported by a NASA Earth System Science Fellowship.

Table of Contents

List of Tables

List of Figures

Abstract

Ozone formation in urban smog is controlled by a complex set of reactions which includes radical production from photochemical processes, catalytic cycles which convert NO to NO_2, and termination steps that tie up reactive intermediates in long-lived reservoirs. The reaction $OH + NO_2 + M \rightarrow HONO_2 + M$ (1a) is a key termination step because it transforms two short-lived reactive intermediates, OH and NO_2, into relatively long-lived nitric acid. Under certain conditions (low VOC/NOx), ozone production in polluted urban airsheds can be highly sensitive to this reaction, but the rate parameters are not well constrained. This report summarizes the results of new laboratory studies of the $OH + NO_2 + M$ reaction including direct determination of the overall rate constant and branching ratio for the two reaction channels under atmospherically relevant conditions:

$$OH + NO_2 + M \rightarrow HONO_2 + M \quad (1a)$$
$$\rightarrow HOONO + M \quad (1b)$$

where the overall rate constant is $k_1 = k_{1a} + k_{1b}$ and the branching ratio is k_{1b}/k_{1a}. Measurements of the pressure dependence of the $OH + NO_2$ bimolecular rate coefficient k_1 have been performed in N_2, O_2, Air and He (50-900 Torr) at 298 K and in Air at 315 K. Measurements of the $HOONO/HONO_2$ branching ratio have been made over the range 50-750 Torr at 298 K. Theoretical calculations of the integrated intensities and correction factors for the HOONO integrated absorbance have been completed. The results of these three studies have been combined to provide fitted fall-off parameters for k_{1a} and k_{1b} over the range of pressures studied at 298 K and 315 K, and recommendations have been made for incorporations in atmospheric chemistry models.

Executive Summary

This project reports a comprehensive experimental examination of the kinetics and mechanism of the reaction of hydroxyl radicals with nitrogen dioxide, i.e.

$$OH + NO_2 + Air \rightarrow HONO_2 + Air \qquad (1a)$$
$$\rightarrow HOONO + Air \qquad (1b)$$

This reaction converts two reactive free radical species (OH and NO_2) into a relatively long-lived species (nitric acid, $HONO_2$) by the predominant product channel 1a. As a result, reaction (1) exerts a large effect on the efficiency of the chain reactions which produce ozone in photochemical smog, and destroy ozone in the lower stratosphere. In the urban atmosphere, reaction 1a is also an important source of nitric acid, which in turn plays a key role in secondary aerosol formation.

The predictions of ozone production in urban airshed models are highly sensitive to the rate coefficients for reactions 1a and 1b, especially under conditions of low VOC/NO_x ratios; however, there is very little available laboratory data in air under relevant conditions of pressure and temperature, leading to significant uncertainty. The principal objective of this project was to reduce these uncertainties by carrying out two separate, but related, laboratory investigations:

Investigation 1: Measurements of the rate coefficient for the overall reaction ($k_1 \equiv k_{1a} + k_{1b}$) under conditions relevant to the urban atmosphere. This work is described under **Task 1** in the narrative summary.

Investigation 2: Measurements of the branching ratio for reaction 1 (k_{1b}/k_{1a}) as a function of total pressure. This work is described under **Task 2** and **Task 3** in the narrative summary.

Taken together, these two investigations provide a new quantitative recommendation for the rate constant for the loss of OH and NO_2 by reaction (1) at ambient atmospheric conditions, and lower the statistical uncertainty. The principal results of the two investigations are summarized below:

Investigation 1: The Pulsed Laser Photolysis-Pulsed Laser-Induced Fluorescence (LP/LIF) technique was used to measure overall rate coefficients (k_1) over the pressure range 50-900 Torr of helium, oxygen, nitrogen and air buffer gases at 298 K and 315 K. This task used the laboratory resources of the NASA/Jet Propulsion Laboratory's Chemical Kinetics and Photochemistry Group. In order to obtain the highest possible accuracy for the rate coefficient determinations, (1) the experiment was designed to operate at high repetition rates, to provide superior sensitivity especially at high air pressures, and (2) the concentration of NO_2 in the LP/LIF reactor was measured directly in the reaction zone, using broad-band UV-visible spectroscopy. The reaction was found to be in the fall-off region between third-order and second-order kinetics. The low pressure- and high pressure-limiting rate coefficients for air buffer gas were found to be:

298 K $\quad k_{0,1}(298\ K) = (1.6 \pm 0.1) \times 10^{-30}$ cm^6 molecule^{-2} s^{-1}

$\quad k_{\infty,1}(298\ K) = (3.0 \pm 0.3) \times 10^{-11}$ cm^3 molecule^{-1} s^{-1}.

315 K $k_{0,1}(315\ \mathrm{K}) = (1.5 \pm 0.1) \times 10^{-30}\ \mathrm{cm^6\ molecule^{-2}\ s^{-1}}$
$k_{\infty,1}(315\ \mathrm{K}) = (2.3 \pm 0.3) \times 10^{-11}\ \mathrm{cm^3\ molecule^{-1}\ s^{-1}}$.

These values may be converted into bimolecular rate coefficients using the fall-off equation given in the narrative summary, which based on the expression used by the NASA Data Evaluation. For the temperature dependence, we recommend a linear interpolation between these two sets of parameters (holding the conventional parameters m and n set to zero). The resulting rate coefficients are 7-15% smaller than the values currently recommended by the NASA and IUPAC data evaluation panels.

Investigation 2: Task 2 involved an experimental determination of the branching ratio between channel (1a) and channel (1b). This is the first study to measure this ratio directly at atmospheric pressures. Experiments were performed with the California Institute of Technology (Caltech) Infrared Cavity Ringdown Spectroscopy (IR-CRDS) apparatus. The products of reactions 1a and 1b ($HONO_2$ and HOONO, respectively) could be detected directly in absorption with this approach. Product yields were measured promptly following pulsed photolysis of gas mixtures over the pressure range 50-700 Torr of nitrogen buffer gas. The infrared absorbances of the products were converted into branching ratios using ratios of infrared band strengths for $HONO_2$ and HOONO derived from the results of high-level quantum chemical calculations. The goal of Task 3 (a collaboration with theoretical chemists at the Ohio State University, Purdue University, and the University of Texas, Austin) was the theoretical determination of these band strength ratios, with ancillary experiments at Caltech performed to test the theoretical model. The branching ratio was found to depend weakly on the total nitrogen pressure. The results were fit to a second-order expression given by:

$$k_{1b}/k_{1a} = (0.0630 \pm 0.0020) + (1.80 \pm 0.18)\times10^{-4}\,P - (1.05 \pm 0.26) \times10^{-7}\,P^2$$

where P is the total pressure in Torr. No temperature measurements were performed, but previous work at low pressure suggests that there is at most a small variation in ratios over the temperature range 298 K to 315 K.

Recommendation for Models

The rate coefficients for the individual channels, k_{1b} and k_{1a}, can be obtained by multiplying the total rate constant $k_1(T)$ from Task 1 by the yield determined from the branching ratio. Due to the rapid decomposition of HOONO back to reactants OH and NO_2 under lower atmospheric (1 atm, room T or higher) conditions, reaction (1b) is effectively a null reaction. Thus, only channel (1a) is relevant, and our reported value of k_{1a} can be used as the effective loss rate of OH and NO_2 to form the sink $HONO_2$. We therefore recommend that only the rate coefficient for formation of nitric acid be used in models:

Reaction 1 - $k_{0,1a}\ (298\ \mathrm{K}) = (1.5 \pm 0.1) \times 10^{-30}\ \mathrm{cm^6\ molecules^{-2}\ s^{-1}}$
$k_{\infty,1a}\ (298\ \mathrm{K}) = (2.5 \pm 0.2) \times 10^{-11}\ \mathrm{cm^3\ molecules^{-1}\ s^{-1}}$

$k_{0,1a}\ (315\ \mathrm{K}) = (1.4 \pm 0.3) \times 10^{-30}\ \mathrm{cm^6\ molecules^{-2}\ s^{-1}}$
$k_{\infty,1a}\ (315\ \mathrm{K}) = (1.8 \pm 0.4) \times 10^{-11}\ \mathrm{cm^3\ molecules^{-1}\ s^{-1}}$

Overall, the rates recommended in this study are somewhat lower than previous estimates and recommendations. It should be noted that this study covers a fairly narrow range of temperatures and pressures which are relevant to the lower atmosphere and cannot be generally extrapolated to all conditions. For the temperature-dependence, we recommend a linear interpolation between the two temperatures studied. Any future revisions of the total rate coefficient k_1, if based on measurements solely of the total reaction, must be multiplied by the branching ratio given above from Task 2. This correction will account for the HOONO channel.

Narrative

Introduction

Ozone formation in urban smog is controlled by a complex set of reactions which includes radical production from photochemical processes, catalytic cycles which convert NO to NO_2, and termination steps that tie up reactive intermediates in long-lived reservoirs. The reaction $OH + NO_2 + M \rightarrow HONO_2 + M$ (1) is a key termination step because it transforms two short-lived reactive intermediates, OH and NO_2, into relatively long-lived nitric acid. For this reason, the spatial and temporal distributions of ozone from urban airshed models are highly sensitive to the rate constants assumed for reaction 1 (k_1). In addition, O_3 isopleths are very sensitive to k_1, particularly at low VOC/NO_x ratios. This has important implications for O_3 control strategies. Russell and co-workers have shown that when the uncertainty in the $OH + NO_2$ rate constant is propagated through an urban airshed model, there is a corresponding uncertainty of 35 ppbv in the calculated O_3 concentration at a downwind site (a 25-50% uncertainty in total O_3).[1] Recent studies have shown that the $OH + NO_2$ reaction can also produce peroxynitrous acid, HOONO, in addition to nitric acid, $HONO_2$.[2-5] Complications arising from this channel introduce an additional 10-30% rate constant uncertainty.

This report elucidates key features of the $OH + NO_2 + M$ reaction including the overall rate constant k_1 and branching ratio for the two reaction channels k_{1b}/k_{1a}:

$$OH + NO_2 + M \rightarrow HONO_2 + M \qquad (1a)$$

$$\rightarrow HOONO + M \qquad (1b)$$

This information is essential to improve the predictive capabilities of urban airshed models with respect to oxidant formation, especially at downwind locations.

Background

Kinetic Rate Parameters

There have been numerous previous studies of reaction 1 using direct techniques. Most of these studies have been carried out in discharge-flow systems at total pressures under 10 Torr.[6-9] A number of studies have employed the flash photolysis, laser photolysis or high-pressure discharge-flow methods which permit higher pressures to be used.[10-21] Many of the high pressure studies encompass the pressure range around 1 atm and two studies focused on the high-pressure limit at pressures exceeding 100 atm[17, 18]. However, there are only three studies that obtained data at 500 Torr and above using N_2 bath gas[10, 14, 15] and only the recent study of D'Ottone *et al.* [15] reached 700 Torr of N_2. *The majority of the previous studies cover the range of conditions appropriate for the upper troposphere and stratosphere but not the urban atmosphere.* The reason for the lack of data at pressures directly relevant to the urban atmosphere is because N_2 quenches electronically excited OH very efficiently. Previous studies using laser-induced fluorescence to measure the relative OH concentration suffer a drastic loss of sensitivity at N_2 pressures near 1 atm, introducing uncertainties into the derived rate constants which are too large to permit a meaningful value to be reported. Table 1 lists the studies which reported rate constants for reaction 1 near 1 atm pressure

of N_2. The bimolecular rate constants at 298 K from the three studies listed in Table 1 are compared in Figure 1.

Table 1 - Previous studies of the OH + NO_2 + M reaction at N_2 pressures of 500 Torr and above.

Reference	Technique	Temp. Range K	N_2 Pressure Range Torr
Anastasi and Smith (1976)	LP/RA	298	5-500
Donahue *et al.* (1997)	DF/LIF	298	2-600
D' Ottone *et al.* (2001)	LP/LIF	273 298	100-700 30-700

LP: laser photolysis, RA: resonance absorption, DF: discharge-flow, LIF: laser-induced fluorescence.

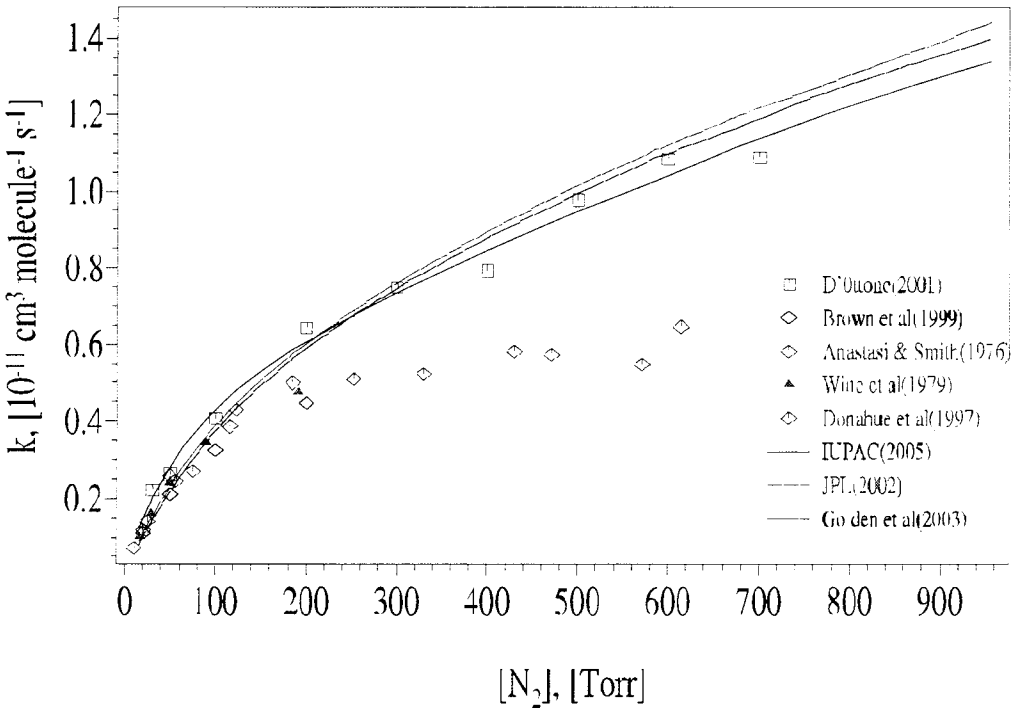

Figure 1 -Comparison of the effective bimolecular rate constant of Reaction 1 in pure Nitrogen at 298 K obtained in the studies listed in Table 1. The rate constant recommendations from the NASA[22] and IUPAC[23] evaluations are also indicated. Rate constants are in cm^3 $molecule^{-1}$ s^{-1}.

The ordinate of these plots is the log of the effective bimolecular rate coefficient k_1, in units of cm^3 s^{-1}. Equation (1) is a termolecular rate law, and the rate coefficient should have units of cm^6 s^{-1}. However, the convention is to subsume the dependence on buffer gas concentration [M] in the termolecular rate expression into the effective coefficient $k_1(T,[M])$.

Figure 1 shows that the rate constant data from the three studies range over about a factor of 2 when extrapolated to 760 Torr total pressure. In particular, the data of the Harvard group, Donahue et al., disagrees substantially from that of D'Ottone et al, the only two studies that provide data above 200 Torr.

Rate constants obtained at specific values of air pressure and temperature are fitted to a semi-empirical expression derived by Troe and co-workers which describes the fall-off behavior for termolecular and unimolecular reactions in the regime in between the low pressure and high pressure limits.[24-26]

$$k([M],T) = \frac{k_0[M]}{1+\frac{k_0[M]}{k_\infty}} F_c^{\left\{1+\left[\left(\frac{1}{N}\right)\log\left(\frac{k_0[M]}{k_\infty}\right)\right]^2\right\}^{-1}} \qquad \text{Eq. 1}$$

where:

- $k_0(T) = k_0^{300}(T/300)^{-n}$, the low-pressure limiting rate constant with units of $cm^6 molecule^{-2} s^{-1}$
- $k_\infty(T) = k_\infty^{300}(T/300)^{-m}$, the high-pressure limiting rate constant with units of $cm^3 molecule^{-1} s^{-1}$
- $N = 0.75 - 1.27F_c$, where the "broadening factor", F_c, can be calculated from expressions derived by Troe and is different, in principle, for every reaction.

The NASA Panel on Data Evaluation recommends a value of

$$F_c = 0.6$$

for every reaction in its tables,[22] while the IUPAC Data Evaluation Panel recommends a value of 0.41.[23] The NASA approach gives satisfactory fits to the experimental fall-off curves for all reactions of atmospheric interest, and the use of a uniform value of F_c simplifies the entry of kinetic parameters in atmospheric models.

In this study we have fit the experimental data to the termolecular fall-off parameters for k_1, assuming the NASA value of F_c=0.6. Additionally, because the current study only determines the rate coefficient curve at two temperatures, we set

$$n = m = 0.$$

Instead values of k_0 and k_∞ are reported specifically for 298 K and 315 K. We recommend that a linear interpolation be made between the two temperatures.

The recommendations of the NASA/JPL[22] and IUPAC[23] data evaluation panels (upon which most atmospheric model calculations are based) for the pressure-dependent rate constant in Nitrogen differ by values greater than 25% in the range of pressures of tropospheric interest. This discrepancy is due to the fact that the IUPAC expression emphasizes a fit to the higher pressure limit obtained in the very high pressure measurements in He obtained by Hippler et al[4], and is a sign of the uncertainty in the data.

There is only one data set available in Air at atmospheric pressures, that of D'Ottone et al.[15]

All studies were done in the pseudo-first-order kinetics regime, with excess NO_2, and uncertainties in the NO_2 concentration measurements typically led to significant systematic uncertainties in the reported rates. In addition, most rate measurements measure loss of OH, and do not explicitly take into account the existence of HOONO formation (with the exception of recent high pressure measurements by Hippler et al.).

Product Branching Ratio k_{1b}/k_{1a}

The existence of HOONO as a minor product of reaction (1) has also played a role in the disagreement between past experiments as it is sometimes ambiguous whether k_1 or k_{1a} was measured. Robertshaw and Smith[20] first proposed the existence of the HOONO channel to resolve a discrepancy in the pressure dependence of reaction (1). The effective bimolecular rate constant k_1 has an anomalous fall-off curve; the observed high pressure rate constant k_1^{∞} is significantly larger than the high pressure limit extrapolated from low pressure data. The discrepancy can be removed if the HOONO channel is insignificant at low pressures, but becomes comparable to the $HONO_2$ channel at high pressures.

The pressure and temperature dependence of k_{1a} and k_{1b} has been modeled by Golden and Smith,[27] Matheu and Green,[28] and Troe.[29] While all three sets of calculations suggest that HOONO formation should compete with the $HONO_2$ channel in the reaction OH + NO_2, the resulting branching ratios at 1 atm and 298 K vary from >1% (Matheu and Green) to 2.5% (Troe) to 30% (Golden and Smith). However, rate constants, fall-off curves, and product yields cannot be calculated quantitatively from first principles, because our knowledge of the transition states, relaxation processes, and potential surfaces (especially for HOONO formation) is too limited. These models rely to some extent on experimental data, and thus cannot accurately predict branching ratios without direct measurements of HOONO.

Direct evidence for formation of HOONO in the gas phase by reaction (1b) has been reported only recently. In 2001, Donahue *et al.*[3] described a series of ^{18}OH isotopic scrambling experiments that support the existence of reaction (1b) and led to an estimate of the low pressure branching ratio of $k_{1b}^0/k_{1a}^0 = 0.17$ at room temperature. Nizkorodov and Wennberg[5] then reported the first spectroscopic observation of gas phase HOONO from the reaction of OH and NO_2 . They reported observation of the $2\nu_1$ overtone spectrum of HOONO formed in a low pressure discharge flow cell using action spectroscopy, detecting OH by LIF after predissociation of the overtone-excited molecules. They observed several bands which they tentatively assigned to the conformers of HOONO and combination bands. They estimated that the HOONO yield was 5±3% at 253 K and 20 Torr. In 2002, Hippler *et al*[4] reported kinetic evidence for channel 1b. They observed a bi-exponential decay in the OH LIF signal in the reaction OH + NO_2 at 5-100 bar and 430-475 K, which they modeled as rapid loss of OH by reactions (1a) and (1b), followed by slower decomposition of HOONO by the reverse rate k_{-1b}. They found the enthalpy of reaction 1b at this temperature range to be $\Delta H_2(0)$= 19.8 kcal/mol, in good agreement with the theoretical predictions of the *cis-cis* HOONO dissociation energy D_0.

In 2002 at the Okumura laboratory at Caltech, Bean et al.[2] made the first spectroscopic measurement of the HOONO/HONO2 branching ratio produced from reaction (1) based on direct infrared absorption detection of the OH stretch fundamental vibrational bands of HOONO and $HONO_2$. They accomplished this by exploiting the exceptionally high sensitivity of infrared cavity ringdown spectroscopy. In those experiments, the HOONO yield formed in a low pressure discharge flow cell was measured to be 8.2+2.0/-2.7% at room temperature and a pressure of P = 20 Torr in a mixture of He, N_2 and other gases. The results are consistent with the recent Golden-

Barker-Lohr calculations. However, they only pin down the low pressure limit, and do not provide information on the rate at atmospheric pressure, which lies in the critical fall-off region. Furthermore, the branching ratios were determined using theoretically computed absorption-cross sections derived in the harmonic limit.

Scope of the Present Work

New experimental measurements have been performed under this Contract, to address directly the deficiencies in the laboratory database for reaction (1) under conditions relevant to the troposphere boundary layer. Specifically:

- Highly accurate measurements of k_1 over a range of conditions relevant to the urban atmosphere (M = air, $273 < T < 310$ K, $50 < P < 900$ Torr) have been carried out with an improved Pulsed Laser Photolysis - Pulsed Laser Induced Fluorescence technique.
- The pressure-dependent branching ratio, k_{1b}/k_{1a} has been measured over a range of conditions relevant to the urban atmosphere (T=298 K, $25 < P <$ 760 Torr).
- High level calculations were performed, including mechanical and electrical anharmonicity, to better estimate the relative HOONO and $HONO_2$ absorption band strengths.

The measured total rates of reaction (1) have been combined with the measured pressure-dependent branching ratio to calculate separate falloff parameters for the individual pathways, k_{1a} and k_{1b}. The work reported here reduces uncertainties in the rate constant for reaction (1).

Task I - OH + NO_2 Kinetics (JPL)

Introduction

The radical termination reaction OH + NO_2 + M → $HONO_2$ + M (1) is an important sink for HO_x and NO_x radicals in the troposphere and stratosphere. Model predictions of tropospheric ozone production and stratospheric ozone loss are highly sensitive to the rate constants of this radical termination reaction. The uncertainty in rate constant for reaction (1) has important consequences for the prediction of tropospheric ozone production and photochemical smog.

There have been numerous previous studies of reaction (1) using different techniques covering the range of conditions appropriate for the upper troposphere and lower stratosphere. There are limited kinetics studies of reaction (1) relevant to urban tropospheric conditions (~760 Torr pressure with M = air, N_2 and O_2). The available rate constants from the previous studies vary by a factor of two. Hence an accurate re-determination of the temperature and pressure dependences of rate constants for reaction (1) is a high priority for atmospheric photochemical model studies.

The main objective of this work is to measure highly accurate rate constants for reaction (1) over a range of conditions relevant to the urban atmosphere (M = air, T = 298 and 315 K). In the present work, the measurement of rate constants have been carried out under tropospheric conditions with an improved Pulsed Laser Photolysis - Pulsed laser Induced Fluorescence technique augmented by in situ optical absorption measurements of NO_2 concentration.

Experimental

The experimental investigation of the title reaction was carried out using the Pulsed Laser Photolysis, Laser Induced Fluorescence (PLP-LIF) technique in which OH radicals are generated by pulsed photolysis of suitable precursors on time scales that are short compared to the subsequent decay, and are detected by laser induced fluorescence.

Pulsed Laser Photolysis-Pulsed Laser Induced Fluorescence

A schematic diagram of the PLP-LIF system is shown in Figure 2. The experiments were carried out using an octagonal stainless steel reaction cell. Gas mixtures entered the mixing column ≈ 30 cm upstream of the photolysis region to ensure proper mixing of the gas. The gas flows were controlled by a gas handling system with calibrated flowmeters. Flowmeters were calibrated volumetrically, by measuring the time rate of displacement of soap bubbles in calibrated volumetric glassware. The accuracy following calibration was ±0.5% (1σ). The temperature inside the reaction cell was measured by using a J-Type thermocouple that could be inserted into the reaction volume where the focus of the telescopic lens system and the laser beams intersect. The pressure in the cell was monitored with 10 and 1000 Torr capacitance manometers over the range of 50 to 900 Torr of buffer gases (Air, N_2, O_2 and He). The capacitance manometers were recently purchased and the factory calibration was used. Pressure readings should be accurate to ±1% (1σ). Typical flow rates, regulated using calibrated mass flow controllers, were between 500 and 1400 sccm, resulting in linear gas velocities

in the reaction cell of > 50 cm s^{-1}. These conditions ensured that a fresh gas sample was photolyzed at each laser pulse, and prevented build up of products.

The laser pump, laser probe and the fluorescence detection axes were mutually perpendicular to each other as shown in Figure 2.

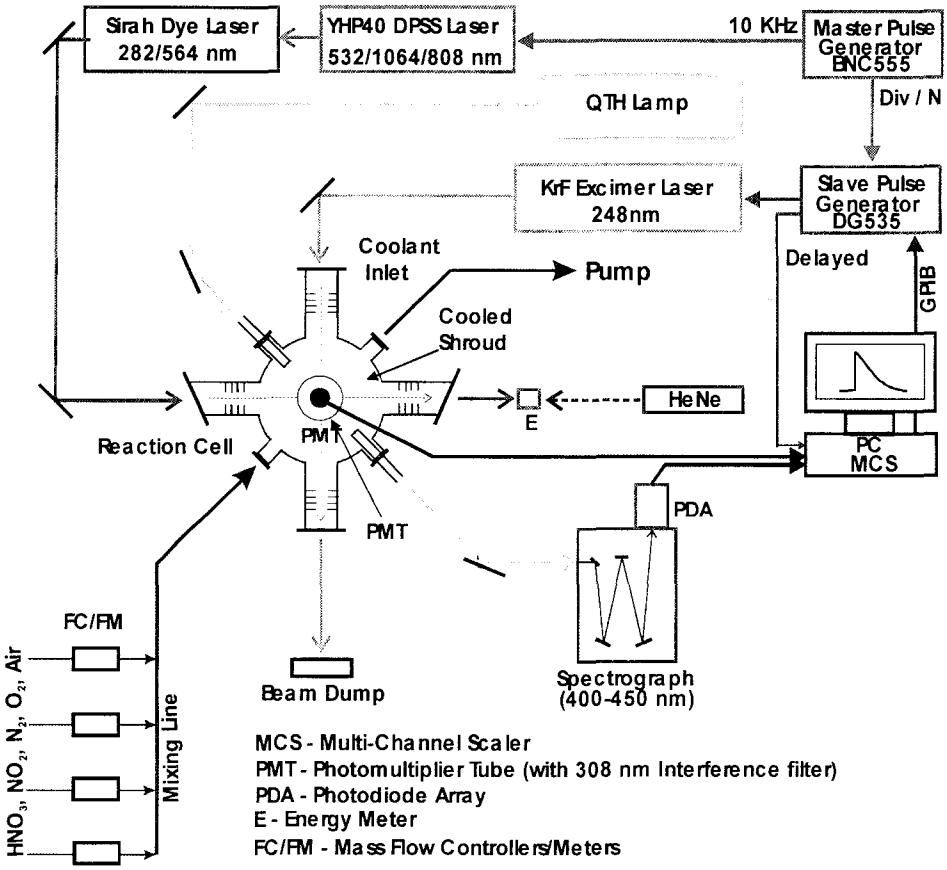

Figure 2 - Schematic diagram of the PLP-LIF system used to study the kinetics of OH + NO_2 +M at high pressures (~800Torr) of Air, N_2, O_2 and He at room temperature.

Generation of OH radicals : The photolysis of $HONO_2$ at 248 nm (KrF excimer laser) was used as the source of OH radicals. The repetition rate of the photolysis laser was 20-30 Hz. Typically, about 10^{15} $HONO_2$ cm^{-3} were photolyzed at a laser fluence of (0.6-1.1) mJ cm^{-2} to generate ≈ (5-10) × 10^{10} cm^{-3} of OH in each photolysis pulse. $HONO_2$ was transported to the photolysis cell by bubbling a 15 -20 sccm flow of Air, N_2, O_2 or He through neat anhydrous $HONO_2$ prepared in the laboratory.

$$HONO_2 + h\nu\ (248\ nm) \rightarrow OH\ (X^2\Pi,\ v = 0) + NO_2 \qquad (2)$$

Detection of OH radicals: The time-resolved OH signal, which was required to determine rate constants for reaction 1, was obtained by laser-induced fluorescence. Excitation of the $A^2\Sigma$ (v = 1) ← $X^2\Pi$ (v = 0), Q_{11} (1) transition at 281.997 nm was achieved using the frequency doubled emission from a diode-pumped solid state (DPSS)-pumped dye laser

(Rhodamine 6G) operating at a pulse repetition rate of 10 kHz. Fluorescence from OH was collected by a lens and baffle system through a 308 nm interference filter and detected by a photomultiplier tube (PMT) operating in photon counting mode. The photon count rate vs. time was recorded by a multi-channel scalar board in a personal computer. In this way, the OH kinetic decay is recorded from each photolysis pulse. This differs from the approach used in most other LP/LIF systems in which the OH signal is measured at a fixed delay time with respect to the photolysis pulse using analog detection. The OH kinetic decay is built up from a series of photolysis pulses with successively longer OH probe pulse delays.

The OH fluorescence is quenched efficiently by N_2, O_2 and air, hence the fluorescence yield and the signal-to-noise ratio degrade as the pressure increases. In the present experimental system, due to the high repetition rate (10 kHz) of the OH probe laser and the use of photon counting detection with enhanced collection efficiency, the OH detection sensitivity is enhanced. These features of the JPL LP-LIF apparatus make it possible to measure rate constants at total pressures of 1 atm and above with high measurement precision.

Optical Absorption measurements of NO_2

The concentration of the excess reactant (NO_2) was determined by in situ optical absorption in the reaction cell. The NO_2 absorption spectrum between 410 -450 nm was recorded by a spectrograph/diode array system with a resolution of ~ 0.2 nm. The concentrations were determined by least-squares fitting of the measured data to a reference UV absorption spectrum[30] degraded to a spectral resolution of 0.2 nm.

Figure 3 shows the measured spectrum, scaled reference spectrum and fit residuals for a typical NO_2 concentration determination using the in-situ spectrometer. The estimated uncertainty of the [NO_2] measurement method was $\leq$ 5% (2σ), with the principal contribution to the uncertainty arising from uncertainties in the absorption cross sections of the reference spectrum.

Nitrogen (99.9993%), Oxygen (99.9993%), Air (99.9993%) and Helium(99.9993%) buffer gases were supplied by Air Products and used without further purification. NO (99%) was supplied by Matheson. NO_2 was synthesized from the reaction of NO with excess O_2 and stored in 20L darkened glass storage bulbs. Anhydrous HNO_3 was prepared in the laboratory from the reaction of $NaNO_3$ with H_2SO_4.

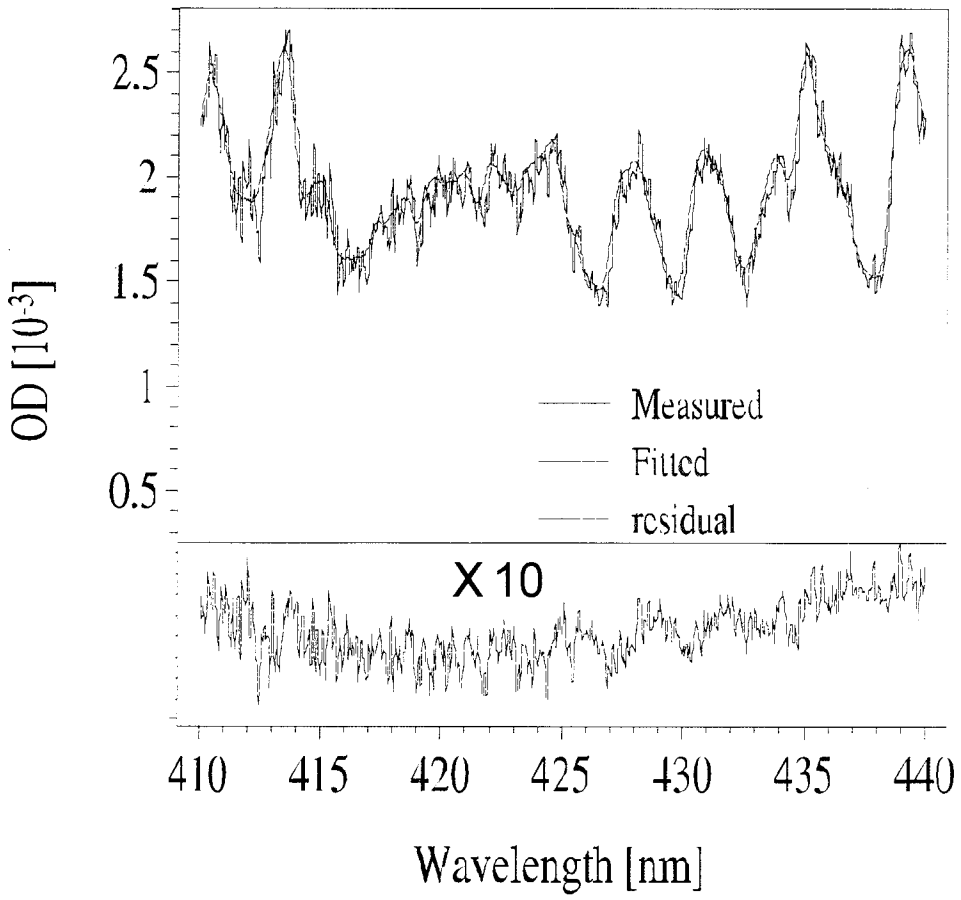

Figure 3 - Spectrum of NO_2 for a typical experiment from the in-situ absorption spectrometer. The upper curve shows the measured (blue) and fitted (red) spectra. The green curve is the residual amplified by a factor of 10. OD = optical density.

Results and Discussion

The PLP-LIF studies were carried out under pseudo-first order conditions with $[NO_2] >> [OH]_0$. The decay of OH is described by:

$$[OH]_t = [OH]_0 \exp-[(k_1[NO_2] + d)t] \quad (3)$$

where $[OH]_t$ is the OH concentration at time t after the laser pulse, k_1 is the bimolecular rate coefficient for the reaction with NO_2 and d is a parameter which accounts for diffusion of OH out of the reaction zone, and reaction of OH with $HONO_2$. The use of low OH concentrations ensures that secondary loss of OH is very low. This was confirmed by showing that the variation of the photolysis laser fluence, and thus radical concentrations, by a factor of three had no measurable influence on the measured first-order OH decay constant.

Overview of Results Figure 4 shows a plot of k_1 versus pressure in M = air, N_2, O_2 at 298 K. The data show pressure dependences that are typical of reactions that are in the fall-off regime between second and third order behavior. The reaction collision

efficiencies vary in the expected manner for these buffer gases (M = air, N_2, O_2) with N_2 being the most effective collisional partner.

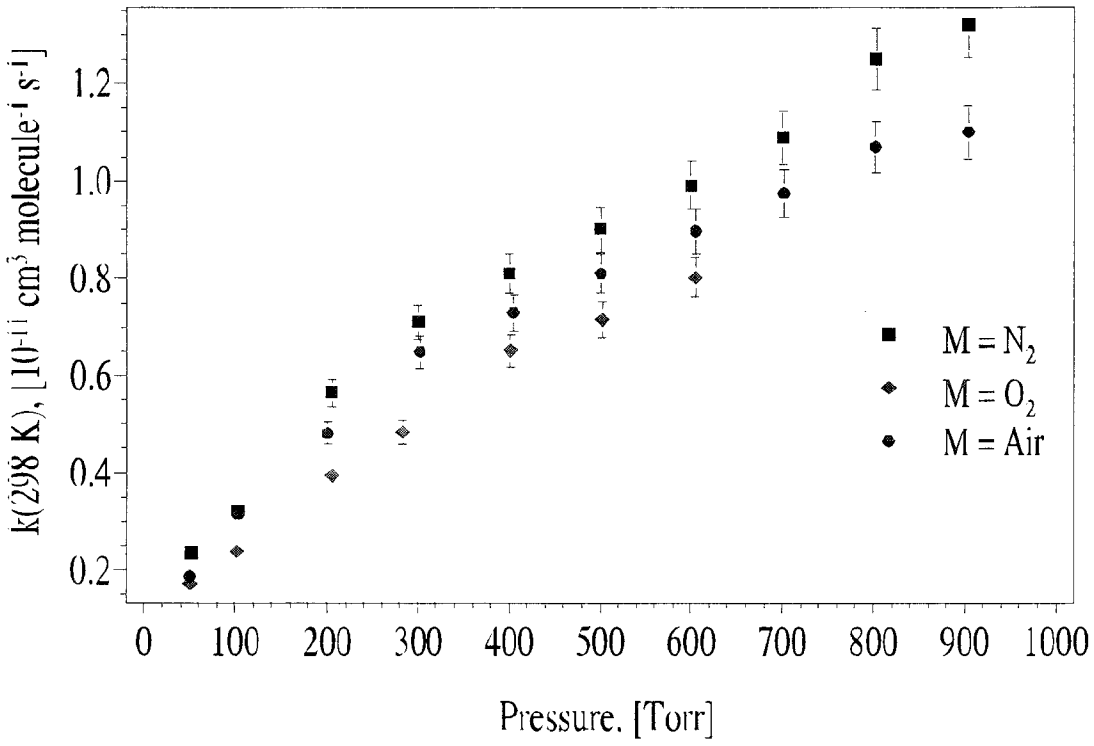

Figure 4 - Fall-off curve for the OH +NO_2 + M (= air) reaction, along with M = N_2 and O_2 at 298 K.

The total error in k_1 at any particular pressure covered in the present work is ≈ 7% and derives mainly from estimated errors in the measurement of the NO_2 concentration, absorptions path length and the fitting error. The 7% error is represented by the vertical error bars at each pressure in Figure 4. The rate constants obtained as a function of buffer gas concentration [M] have been fitted to a semi-empirical expression derived by Troe and co-workers which describes the falloff behavior for termolecular and unimolecular reactions in the regime in between the low pressure and high pressure limits[10, 13, 15]in Eq. (1), as described above in the Introduction. In the present study, the NASA value of F_c=0.6 has been assumed.

Nitrogen at 298 K

Our measurements carried out in N_2 buffer gas are compared with prior studies [10, 13-15, 21] and the NASA/JPL 2002[22], IUPAC 1997[23] recommendations in Figure 5 over the pressure range 50-900 Torr. At pressures below 100 Torr, the data sets agree within the respective error bars. Above 200 Torr, there are two distinct set of data. Our measurements lie approximately 10% lower than the data of D'Ottone et al[15] and 20% above the data of Brown et al, Wine et al, and Donahue et al. [13, 14, 21]

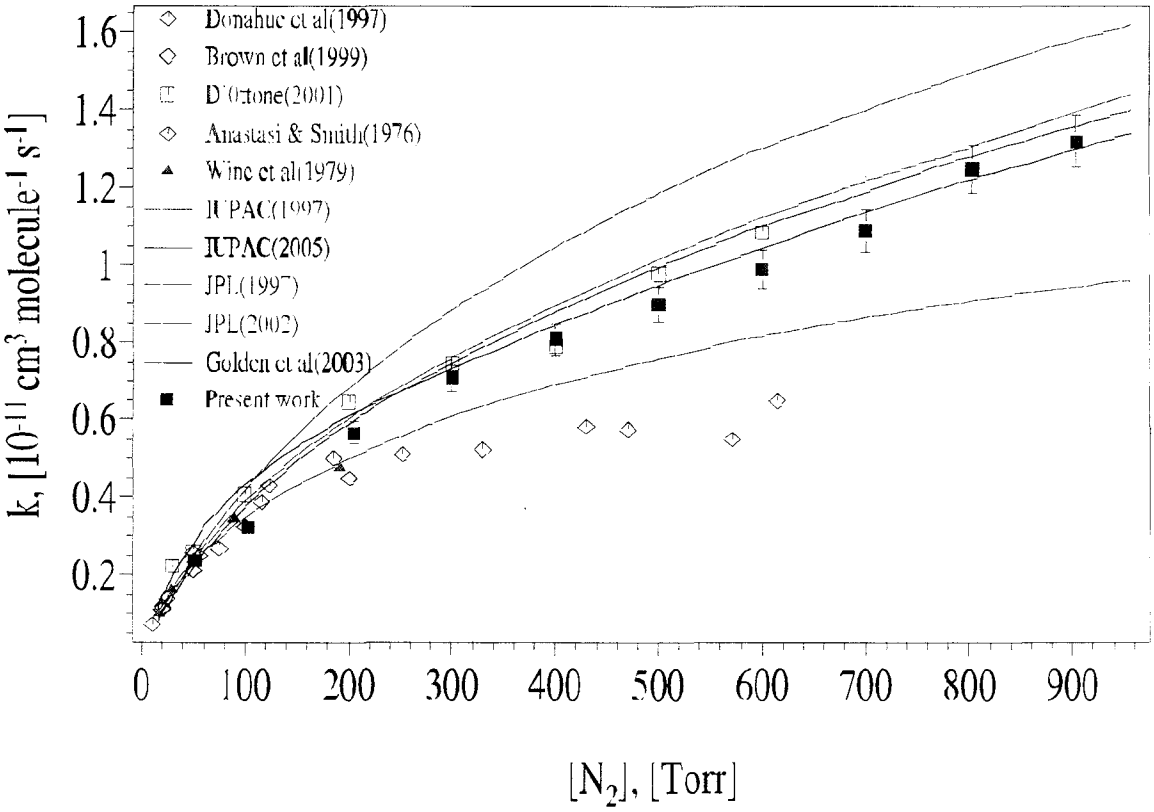

Figure 5 - Plot of our second order rate constants (k_1) for OH + NO_2 in N_2 at 298 K compared with literature data.

Most of the previous measurements in N_2 buffer gas have been limited to 250 Torr,excluding the measurements of D'Ottone et al[15] and Donahue et al[14, 31] whose data extended to 700 Torr of N_2. In the present experiments, we have extended the fall-off curve to 900 Torr of N_2 and air. Table 2presents a comparison of the various kinetic methods and NO_2 measurement techniques employed in previous studies. The measurements of D'Ottone et al [15] used the PLP-LIF technique which is similar to the present work while Donahue et al[14] used the high pressure flow tube technique. Comparing our data with that of D'Ottone et al [15] over the pressure range of 50 – 900 Torr in N_2 bath gas, a discrepancy of 10% is observed. This is possibly related to the differing methods for the measurement of [NO_2], the principal source of uncertainty in the rate constant determination. As shown in Table 1, D'Ottone et al [15] used external absorption cells located upstream and downstream of the reaction cell to measure [NO_2].

The absorption measurements were carried out with a Hg lamp monitoring the absorption at a single wavelength (365 nm). In the present experiment, we measure the NO_2 concentration inside the reaction cell rather than outside the cell. Also we record the absorption spectrum between 410 to 450 nm using spectrograph and photodiode array which enables the entire spectrum to be fitted instead of a single wavelength. With this technique, we avoid errors due to intensity drift in the light source. Also, the signal-to-noise of the measurement is significantly enhanced due to the multiplex advantage.

Above 200 Torr pressure, the NASA/JPL 2002[22] and IUPAC 1997[23] recommendations overestimate our data by 10%-25%. The recent IUPAC (2005) recommendations for $M = N_2$ are in excellent agreement with the present data. A fit of our data in $M = N_2$ to the JPL formulation of the three-body fall-off expression gives N_2:

$$k_{0,1}(298\ K, N_2) = (1.7 \pm 0.1) \times 10^{-30}\ cm^6\ molecule^{-2}\ s^{-1}$$
$$k_{\infty,1}(298\ K, N_2) = (3.4 \pm 0.3) \times 10^{-11}\ cm^3\ molecule^{-1}\ s^{-1}$$

compared with values $k_0 = 2.0 \times 10^{-30}\ cm^6\ molecule^{-2}\ s^{-1}$ and $k_\infty = 2.5 \times 10^{-11}\ cm^3\ molecule^{-1}\ s^{-1}$ recommended in NASA /JPL 2002.

Table 2- Summary of literature measurements of $OH + NO_2 + M$
FP/RF - Flash Photolysis/Resonance Fluorescence
FP/RA - Flash Photolysis/Resonance Absorption
PLP/LIF - Pulsed Laser Photolysis/Laser Induced Fluorescence

Ref.	Method	Location of absorption measurement	NO_2 calibration
Wine *et al* (1979)	FP/RF	External absorption cell	Hg lamp(365nm)
Anastasi & Smith (1976)	FP/RA	-------	From measured mole fraction
Brown *et al* (1999)	PLP/LIF	External absorption cell	Hg lamp(365nm)
Donahue *et al*(1997)	HP-DF/LIF	External absorption cell	Indirect (using tracer)
D'Ottone *et al* (2001)	PLP/LIF	External absorption cell	Hg lamp(365nm)
This work	PLP/LIF	Inside the reaction cell	Spectral fitting between 410 - 440nm

Oxygen at 298 K

Figure 6 shows our measurements in M= O_2 (298 K) over the pressure range 50 -600 Torr compared with the data from previous studies. Our data agree with the results of D'Ottone et al[15] at pressures below 200 Torr. Above 200 Torr, our data are about 5% lower than the data of D'Ottone et al. The room temperature data in M = O_2 compared with N_2 is shown in Figure 4. As is consistent with previous work, we find that molecular oxygen is a less efficient stabilizer, leading to lower (5-20%) bimolecular rate constants.

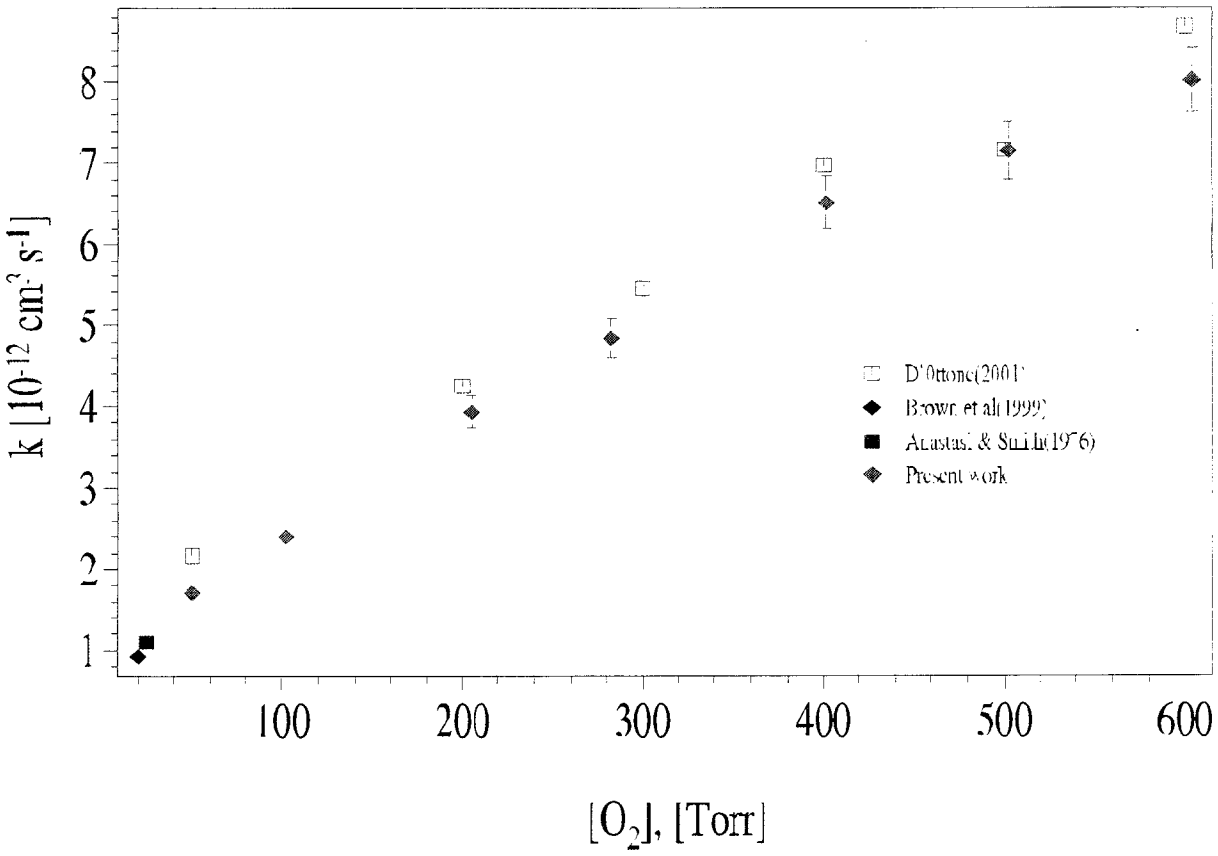

Figure 6 - Plot of our second order rate constants (k_1) for OH + NO_2 in O_2 at 298 K compared with literature data

Air at 298 K

Our measurement in M = air at 298 K compared with D'Ottone et al. is shown in Figure 7. Again, our results are lower than the data of D'Ottone et al [15] by 10-15%. A fit of our data M = air to the JPL formulation of the three-body fall-off expression would give $k_0 = (1.6\pm 0.1) \times 10^{-30}$ cm^6 molecule^{-2} s^{-1} and $k_\infty = (3.0\pm 0.3) \times 10^{-11}$ cm^3 molecule^{-1} s^{-1}.

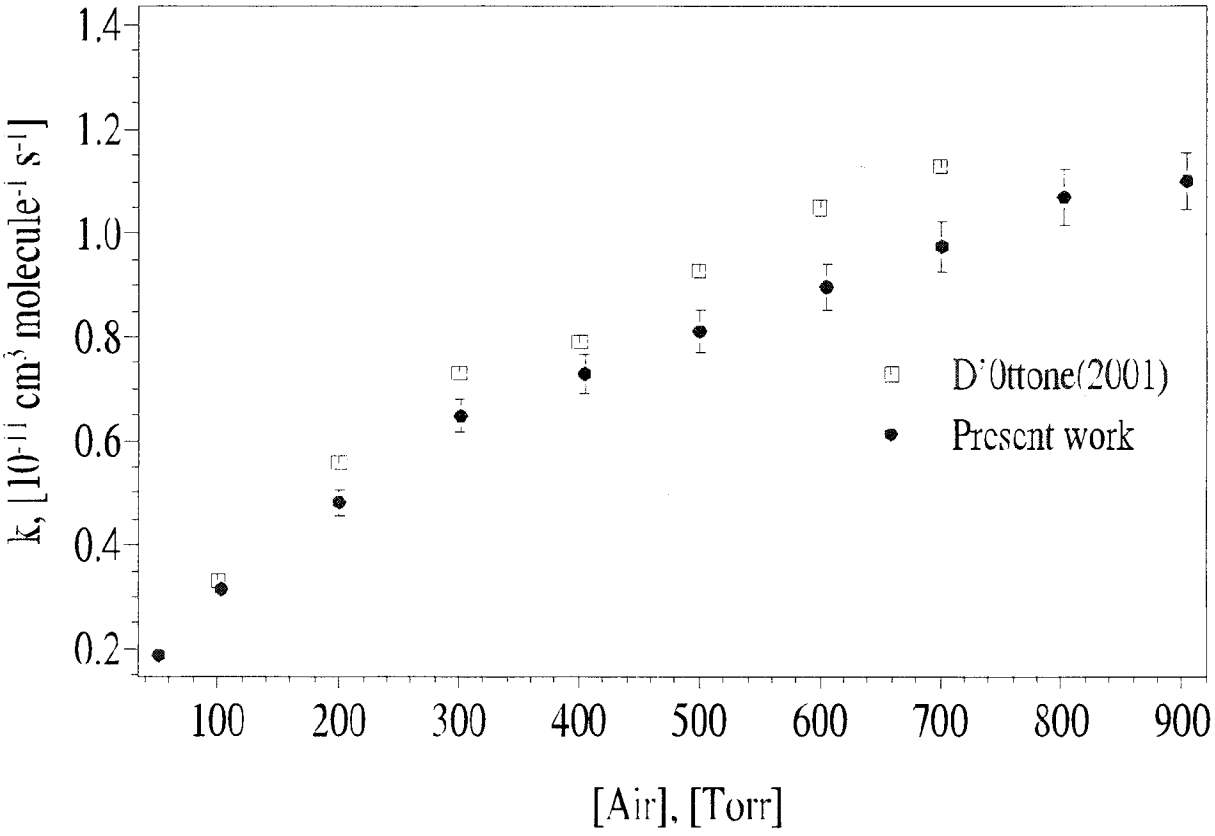

Figure 7 - Plot of our second order rate constants (k_1) for OH + NO_2 in Air at 298 K compared with literature data.

Air at 315 K

Measurement of rate constants in M= air were carried out above room temperature (315 K). A comparison of the 298 K and 315 K data is shown in Figure 8. These data are fit to the fall-off expression, yielding: $k_0 = (1.5\pm 0.1) \times 10^{-30}$ cm^6 molecule^{-2} s^{-1} and $k_\infty = (2.3\pm 0.3) \times 10^{-11}$ cm^3 molecule^{-1} s^{-1}.

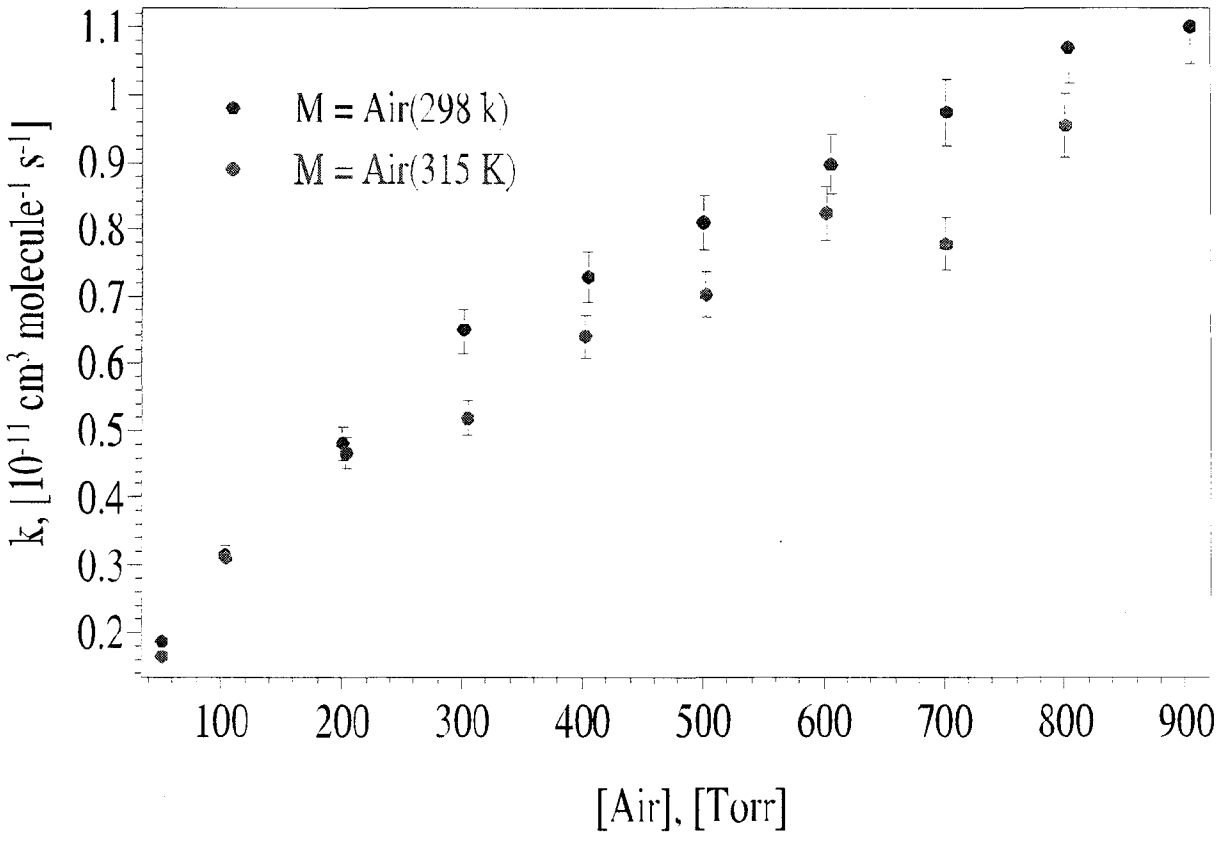

Figure 8 - Plot of our second order rate constants (k_1) for OH + NO_2 in Air at 315 K compared with the room temperature data.

Helium at 298 K

We performed additional measurement in M = He at room temperature, because the most extensive studies of the pressure dependence of reaction 1 have been done in helium. Quenching of LIF signal from He is substantially lower, so far more data is available over a wider pressure range. Figure 9 shows a comparison of the pressure dependence obtained in the work together with prior studies in helium. Over the range of pressures studied here, 50 – 900 Torr, the agreement between our data and prior studies is quite good including the data point at 300 Torr reported by Forster et al.[17] Extrapolation of our data above 1000 Torr, M = He appears to be somewhat less consistent with the data obtained in the high pressure experiments (1 -150 atm) of Forster et al. [17] (scaled down by the later correction factor of Hippler et al.) and of Hippler et al.[4] The good agreement with experiments at similar pressures provides additional confidence that our approach is sound.

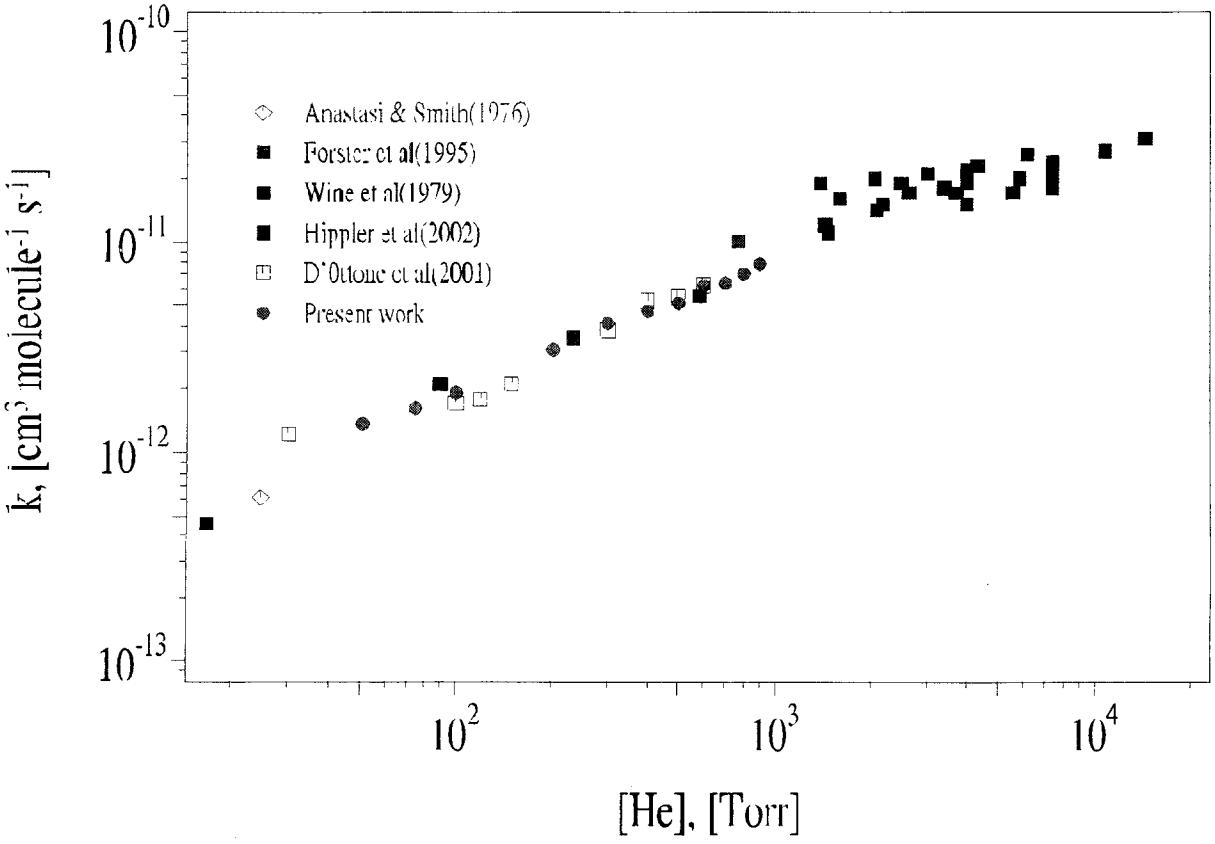

Figure 9 - Plot comparing our measurements of $k_1(298)$ in He with literature data.

Summary and Implications

In the present experiment, OH + NO_2 +M rate constants in N_2, O_2, air and He at 298 K and 315 K have been measured under urban tropospheric conditions. The overall uncertainty in the measured rate constant is estimated to be ~ 7%. Our results are significantly lower than the NASA/JPL 2003[22] and IUPAC 1997[23] recommendations at pressures above 200 Torr, but are in excellent agreement with the IUPAC 2005 recommendations. Our results in N_2, O_2 and Air show measurably different third-body efficiencies in the range of pressure between 50 and 800 Torr, O_2 being less efficient than N_2. Our results in He are in good agreement with the data of Anastasi & Smith[32], D'Ottone et al[15] and Wine et al[21] but are considerably different from the very high pressure measurements of Hippler et al[4] and Forster et al[17]. Future experiments will extend these measurements to low temperature.

The three body recombination rate in air in the present study is consistently lower than prior literature data. At pressures relevant to the lower troposphere (~700 Torr) in air, the recombination rate differs by 15 - 20%. This lowering of the rate constants for this reaction 1 as seen in the present study would increase the efficiency of the HO_x-driven catalytic ozone destruction cycle in the stratosphere. In the troposphere, the observed decrease in the rate constant at pressures near 1 atm will result in increased ozone formation. Since our experiments in Task II indicate that HOONO decomposes slowly compared to the measurement time in this experiment (see below), the measurements here are determinations of the total loss of OH from reaction 1, $k_1 = k_{1a} + k_{1b}$.

Task II - $HOONO/HONO_2$ Branching Ratio (Caltech)

Introduction

The importance of the reaction $OH + NO_2 + M$ in the troposphere, and especially polluted urban environments, stems from its production of nitric acid ($HONO_2$). Nitric acid is a stable molecule which acts as a sink for HO_x and NO_x radicals, both of which are critical to the formation of photochemical smog. It has been well documented in the past few years that, in addition to nitric acid, reaction 1 also produces the less stable peroxynitrous acid (HOONO) [2, 4, 5, 14]. HOONO is weakly bound (19.6 kcal/mol), and re-dissociates rapidly under atmospheric conditions. HOONO thus does not act as a sink for HO_x and NO_x, and the effective loss rate is determined solely by the rate coefficient k_{1a}. As a result, the interpretation of the measured total rates of reaction 1 for the purposes of airshed modeling should explicitly take into account the branching ratio of HOONO to $HONO_2$.

This branching ratio has been measured previously at 20 Torr of a $He/H_2/N_2$ mixture by using infrared cavity ringdown spectroscopy (IR-CRDS) to measure the integrated absorbance of both $HONO_2$ and HOONO[2]. The most stable conformer HOONO is the *cis-cis* isomer. Studies show that this isomer is the only one present at room temperature.[33] The OH stretch frequency of *cis-cis* HOONO is shifted 250 cm^{-1} to the red of $HONO_2$ by an internal hydrogen bond, thus providing a unique spectroscopic signal for the two molecules. The high sensitivity of cavity ringdown is ideal for this measurement due to the low concentrations of HOONO. By coupling a pulsed ringdown apparatus to a photolysis cell for the generation of OH radicals, the HOONO branching ratio can be measured over a wide range of atmospherically-relevant pressures.

Basic Approach

In this work, we initiate the radical chemistry by laser photolysis of a gas mixture containing OH precursors in the presence of NO_2. This approach is in contrast to the previous branching ratio determination by our group, in which we used a low pressure discharge flow method to generate OH. The photolysis method allows us to produce sufficient OH at high pressures in a clean manner. All kinetics were modeled to take into account secondary chemistry.

We again use IR-CRDS for product detection, because it provides superior sensitivity, approximately two to four orders of magnitude better than conventional absorption methods with time resolution of 10-100 μs. The high temporal resolution allows us to look at products promptly, after reaction has been completed but well before secondary reactions, diffusion, or wall losses, can change the apparent product concentrations.

Product abundances are determined by obtaining the complete ν_1 (OH stretch) band in the infrared for both HOONO and $HONO_2$ at each pressure, and integrating to obtain the band absorbance. The spectral resolution is sufficient to identify unambiguously the contribution of each species, even in the presence of interference from background, either baseline effects or absorption by other molecules. The actual concentrations are derived using our best theoretical estimates of the relative HOONO and $HONO_2$ ν_1 band strengths (see Task 3).

The primary complications are the following:

- The radical concentrations are fairly high (and atypical of the natural atmosphere), but all relevant reaction rates are well known and the secondary chemistry can be modeled. Experimental conditions were designed to ensure the least bias due to secondary reactions. Furthermore, unlike solution phase chemistry, the collisions are predominantly still in the bimolecular regime. Even at 1 atm, the duration of a collision (picoseconds or less) is 100 to 1000 times shorter than the mean time between collisions (order of 1 nanosecond), which will be dominated in any case by collisions with the buffer gas.
- The OH is initially produced with an excess of vibrational energy. Under the conditions of the current experiment, the OH should be relaxed to thermal temperatures. As a check, we have performed additional experiments adding SF_6 (a good vibrational quencher) and used alternate chemistry (reactions involving CH_4).
- Since we elected to form OH by chemistry that also initially involved H atoms, we were unable to perform the experiments in the presence of O_2. Some H atoms could recombine to form HO_2.
- In order to convert from our measured integrated absorbances for the two species to relative concentrations, we rely on calculations of the ratio of their integrated absorption cross sections. These calculations are discussed in detail in Section III below.
- The use of IR-CRDS to measure the branching ratio introduces a further complication: Integrated intensities measured by cavity ringdown methods when the linewidth of the laser is larger than that of the absorber (such as ours) have been shown to be quantitative only for very small absorbances[34-36] and are nonlinear at high absorbances. The HOONO measurements fall in the small absorbance limit, but the large $HONO_2$ absorbances generated in these experiments fall outside the linear regime of our CRDS apparatus. We carried out calibration experiments for the nitric acid band as a function of pressure and concentration so that our observed integrated absorbances could be corrected to represent the true integrated absorbance of $HONO_2$.

Methods and Materials

Photolysis and Chemistry

We initiated the reaction OH + NO_2 + M via the following reaction scheme.

$$O_3 + h\nu(248nm) \rightarrow O(^1D) + O_2 \quad (3)$$

$$O(^1D) + H_2 \rightarrow OH + H \quad (4a)$$

$$H + NO_2 \rightarrow OH + NO \quad (5)$$

$$OH + NO_2 + M \rightarrow HONO_2 + M \quad (1a)$$

$$\rightarrow HOONO + M \quad (1b)$$

Both reaction 4a and reaction 5 are known to produce OH with a high degree of vibrational excitation.[37] As a result, some experiments were carried out with the OH production from the reaction

$$O(^1D) + CH_4 \rightarrow OH + CH_3 \quad (4b)$$

While this chemistry was an efficient and clean way to make OH with few unwanted byproducts, it required a system free of O_2 to prevent the rapid formation of HO_2. As a result, the branching ratio measurements were all done in a gas mixture which was mostly N_2 (>90%) with the remainder essentially all H_2. While these measurements could not be carried out in air, the branching ratio is not expected to have a significant dependence upon the nature of the bath gas.

Ozone was produced from an ozonizer (Osmonics V10-0) and then trapped on silica gel (6-12 mesh) at -78^{0}C. The ozone was then delivered to the cell by flowing nitrogen across the silica gel. The concentration of ozone in the nitrogen flow was measured by 248nm absorption through a 1cm quartz cell upstream of the reaction cell and was stable over the course of a day. Hydrogen and methane were introduced as pure gas flows. NO_2 was introduced as a 4% mixture in nitrogen (Matheson). All reactant gases and a nitrogen dilution flow were mixed in a glass cross about 5 cm from the photolysis region. All gas flows were through calibrated mass flow transducers (Edwards Model 831 and Omega Model 1700) so that final concentrations in the photolysis cell could be calculated. Calibration was performed as described above in Task I and did not influence our branching ratio measurements. Concentrations of the reactant gases were varied systematically to check for any unexpected correlations. Typical concentrations used for the pressure-dependent measurements are listed in Table 3.

Table 3- Concentrations used in HOONO/$HONO_2$ Branching Ratio Measurements

Gas	Concentration range / molecules cm^{-3}
O_3	$1\text{-}10\times10^{15}$
NO_2	$1\text{-}10\times10^{16}$
H_2	$1 - 10\times10^{17}$
N_2	balance to pressure

The apparatus used for these measurements was a gas flow cell which combines pulsed laser photolysis for the initiation of chemistry and pulsed infrared cavity ringdown spectroscopy for the detection of products (see Figure 10). The general design uses a rectangular photolysis cell which is coupled on both ends to Teflon blocks. These blocks provide feedthroughs for gas inputs, a pumpout port and pressure gauges, and serve to link the photolysis cell to the ringdown mirrors. Pressures were measured with capacitance manometers which had recently been calibrated relative to calibration standards at JPL and were therefore accurate to ±1% (1σ).

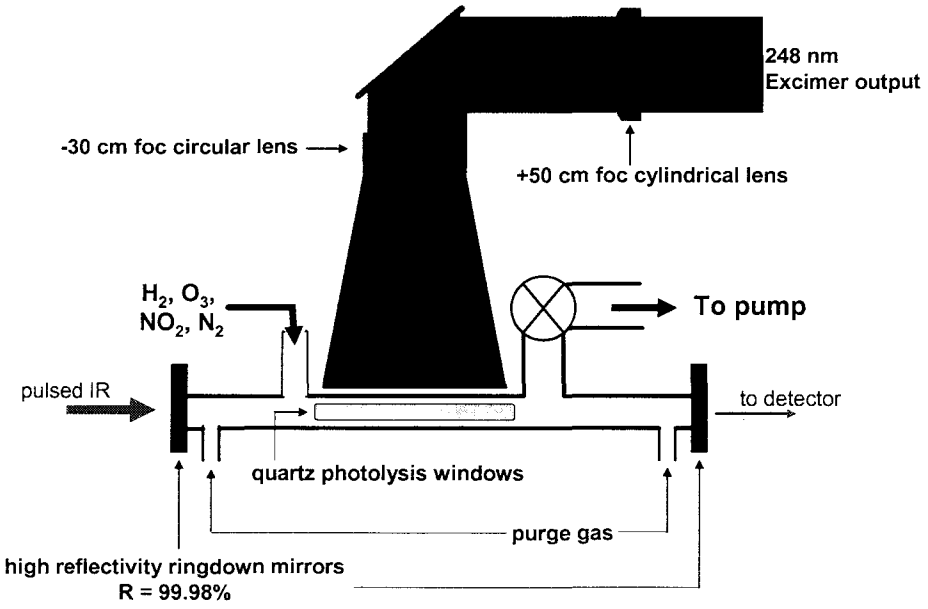

Figure 10 - Schematic of apparatus used for HOONO/$HONO_2$ branching ratio measurements

Three photolysis cells with different lengths were employed for the experiments. Progressively longer cells were fabricated to study the impact of lower initial radical concentrations while maintaining reasonable signal to noise. The shortest cell was made entirely of quartz and was 3 cm long with interior dimensions of 1cm x 1cm. The other two cells were made from square stainless steel tubing (1cm x 1cm inside) with Suprasil windows glued onto cut-out sections on the sides. One cell was 7.5 cm long with a 6 cm photolysis window. The other was 13.5 cm long with a 10 cm photolysis window. In both cases the photolysis windows were epoxied to the cells with Torr Seal. Both stainless steel cells were coated with FluoroPel polymer to minimize interactions between the reagents and the cell walls.

Photolysis was initiated with the 248 nm pulse from a KrF excimer laser. The output beam was a slightly diverging 1cm x 2.5 cm rectangle but was subsequently reshaped using a +50 cm focal length cylindrical lens and -30 cm focal length circular lens to match the width of our photolysis window on the long axis of the beam and create a gently focusing 2-5 mm beam along the short axis. The laser flux was varied over the range $1\text{-}50\times10^{15}$ photons cm^{-2} to test for any possible dependence of the measured branching ratio on the photolysis energy.

Detection of Reaction Products

Absorption spectra of the reaction products were recorded by pulsed cavity ringdown spectroscopy.[38-40] A mid-infrared laser pulse was injected into an optical cavity made by two high-reflectivity infrared mirrors (R = 99.98%, centered at $\lambda = 2.8$ μm, 6 m radius of curvature) sealed to the ends of the detection cell. Each mirror was separated from the main flow of gas by a purge volume approximately 15 cm long.

Nitrogen flowed over the mirrors and through the purge volumes to protect the mirrors and to minimize losses in reflectivity due to deposition.

We produced tunable (2.7-3.3 μm) mid-IR in a two-stage optical parametric amplifier (OPA) by mixing the second harmonic of an Nd:YAG laser and the output of a tunable dye laser (DCM laser dye) in a pair of KTP crystals.[41] The OPA produced an IR beam with energy E ≈ 1 mJ/pulse and diameter d ≈2 mm after transmission through three filters to remove the residual 532 and 630 nm light. The IR linewidth was $\Gamma \approx 1$ cm^{-1}. The IR wavelength was typically calibrated using the frequencies of known HONO and $HONO_2$ peaks in the spectrum. The IR beam was sent through a series of two irises and a +1 m focal length lens to improve the beam quality and then aligned into the cavity. The residual beam exiting the cell was focused tightly onto a 1-mm diameter InSb detector (Infrared Associates). Each ringdown trace was amplified and then accumulated with a 50 MHz bandwidth digital oscilloscope card with 14-bit digitizer (GageScope 1450). For each point in a spectrum, typically 16 ringdown traces were averaged and then fit to a single exponential function and constant baseline by the Levenberg-Marquardt algorithm.[42]

The ringdown lifetime of radiation trapped in an evacuated optical cavity of length L with mirrors of reflectivity R is $\tau_0 = L/c(1-R)$, where c is the speed of light.[43-45] Typical empty-cell ring-down times were $\tau_0 \approx 10$ μs, in good agreement with the stated mirror reflectivities (99.98% at the peak wavelength). In the presence of an absorber, the lifetime is given by $\tau = L/c(1-R+\alpha L_S)$, where $\alpha = [X]^*\sigma_X$ is the extinction coefficient of the absorber X and L_S is the absorption path length through the sample. The measured extinction coefficient is then

$$\alpha = \frac{L}{cL_S}\left(\frac{1}{\tau} - \frac{1}{\tau_0}\right)$$

Spectra of reaction products were typically recorded by scanning the spectral region of interest alternating 16 shots with the excimer on and then 16 shots with the excimer off and then subtracting the two. This subtraction eliminated background due to species present in the absence of reaction, as well as to the wavelength-dependent ringdown loss of the mirrors. The movement of the dye laser and OPA as well as the collection, averaging, and fitting of ringdown traces are controlled by a program written in Labview. Excimer on-excimer off spectra were then fit with reference spectra of all known bands in the region of interest and the integrated absorbance of the ν_1 bands of $HONO_2$ and HOONO measured.

$HONO_2$ Calibration Experiments: The correction factor (1+f)

The ν_1 band of nitric acid has a highly congested spectrum containing many very sharp features. The apparent cross section of our ringdown apparatus for such a species at large concentrations is likely not constant due to a systematic under-emphasis of the narrowest and strongest features when the ringdowns are fit to a single exponential function. In order to correct our measured integrated absorbances so they reflect the true concentration of nitric acid, correction factors have been derived both theoretically and experimentally.

A program has been written which convolves an assumed high resolution spectrum and laser profile into an effective multi-exponential CRDS decay at each

spectral point. These multi-exponential decays are then fit to a single exponential by the same algorithm used in our CRDS experiments. For our assumed spectrum we used the Doppler-limited FTIR spectrum of nitric acid obtained from Goldman and Pine, as shown in Figure 11, pressure broadened with Lorentzian lineshapes to various pressures. The results shown here assume a Gaussian laser profile with FWHM = 1.0 cm^{-1}, shown in the top portion of Figure 11, although the results were insensitive to the precise shape and width of the assumed laser profile. To make quantitative comparisons to our experimental results it was also necessary to assume $\sigma_{obs} = 1.23\times10^{-17}$ cm $molecule^{-1}$ for the ν_1 integrated intensity and a typical background $1/\tau_0 = 144000\ s^{-1}$.

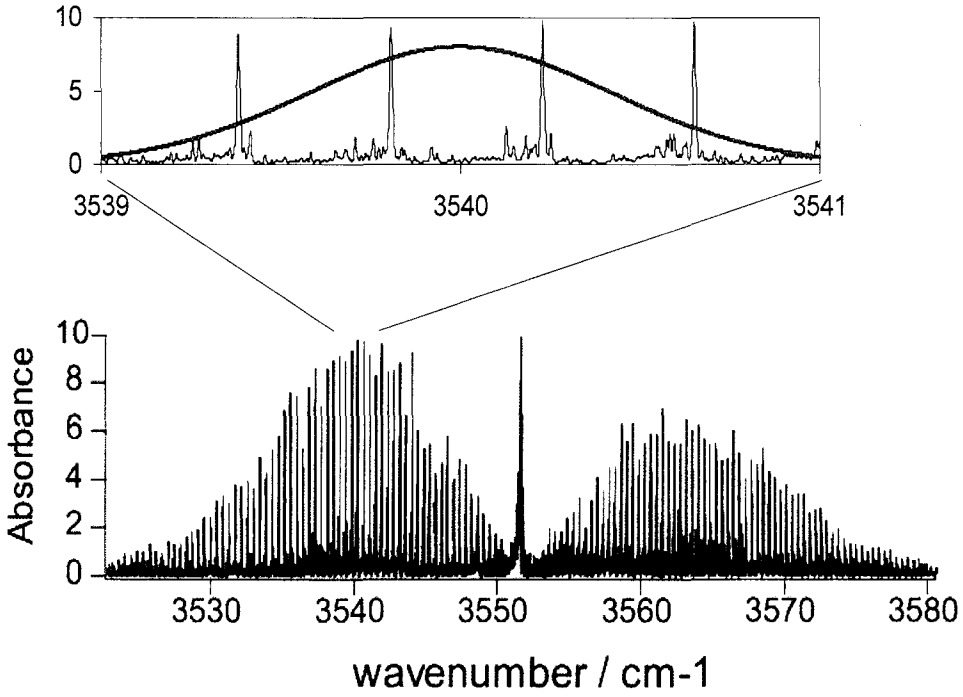

Figure 11 - Spectrum used for CRDS simulations of the $HONO_2$ ν_1 integrated absorbance. Inset shows an expanded portion of the spectrum with the Gaussian laser profile used shown in grey.

A schematic of the apparatus used to verify the results of these calculations is shown in Figure 12. Nitric acid was introduced by flowing N_2 through a temperature-controlled bubbler containing pure nitric acid. The nitric acid flow was diluted with N_2 before entering the first flow cell (Cell A) where the concentration was measured by direct UV absorption. The nitric acid concentration was then further diluted with N_2 before entering the second flow cell (Cell B) where the absorption to be calibrated is measured with IR-CRDS. The ringdown mirrors, data collection, and fitting of ringdown

traces for these experiments were identical to those described above.

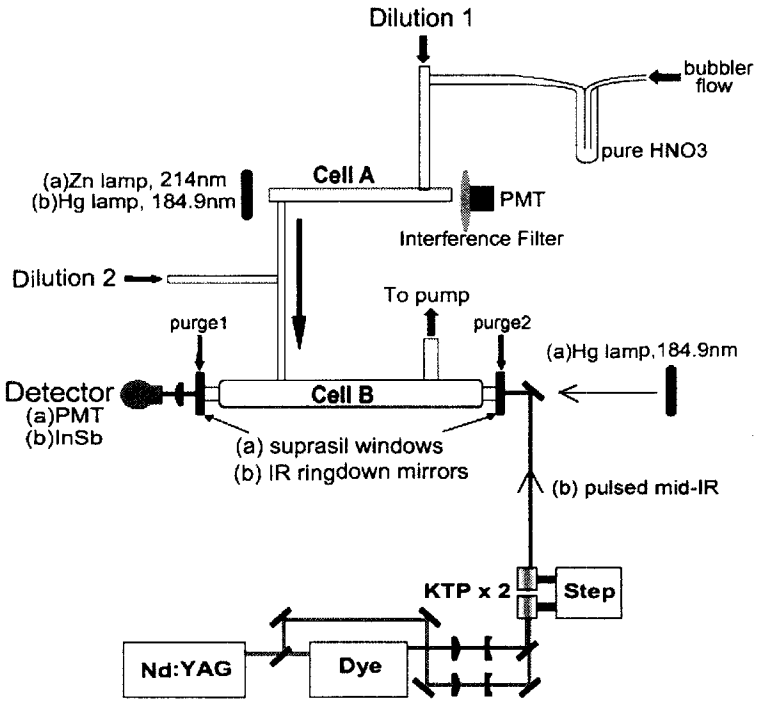

Figure 12 - Schematic of the apparatus used for $HONO_2$ ν_1 integrated intensity calibration experiments.

Cell A was 30.2 cm long with an inside diameter of 1.0 cm and UV-grade quartz windows glued to the ends. The nitric acid concentration was measured in Cell A by UV absorbance at 184.9 nm. 184.9 nm radiation is produced by an Hg pen-ray lamp (UVP), collimated through a series of lenses and irises, passes through cell A, and is detected with a PMT using a 184.9 nm interference filter to eliminate detection of 254 nm radiation. The second flow cell, cell B, was the same as for the ringdown apparatus described above, but with the photolysis cell in the center replaced by a glass flow cell. The center of cell B, which contained the nitric acid, was 18.0 cm long with an inside diameter of 2.0 cm. The total mirror-mirror length of Cell B was 47 cm, but had purge flows of N_2 over the ends to prevent the high reflectivity ringdown mirrors from interacting with nitric acid.

The effective pathlength of sample, L_s, was measured independently under the flow and pressure conditions used in these experiments in order to quantify diffusion from the sample region into the purge volumes. The apparatus used for measuring Ls was identical to Cell B described above, but with the CRDS mirrors replaced with UV-grade quartz windows.

All flows are measured with Edwards mass flow transducers. The transducers were calibrated volumetrically by measuring the displacement of soap bubbles at various flow rates. The estimated accuracy following calibration was ±0.5% (1σ). The pressure is measured from ports in the center of both cells using MKS Baratron capacitance manometers. The manometers were calibrated relative to standardized calibration heads at JPL. The estimated accuracy following calibration was ±1.0% (1σ).

The nitric acid used was synthesized by adding concentrated H_2SO_4 to $NaNO_3$ under vacuum and collecting the nitric acid vapor in a liquid N_2 cold trap. When not being used the sample was stored in a liquid N_2 dewar. After storage, the sample would contain small quantities of the decomposition product NO_2. After bubbling for about 5 minutes, the NO_2 would completely degas leaving pure nitric acid. This process was confirmed by connecting our flow system to a Nicolet FTIR spectrometer and monitoring the NO_2 absorption in time. All tubing, valves, and joints between and including Cell A and Cell B were either glass or Teflon to minimize surface decomposition. All nitrogen used was flowed through a sieve trap to ensure the complete removal of trace water.

Results

A sampling of the results of our $HONO_2$ calibrations is shown in Figure 13. The calculations and experiments were in good agreement. Both showed the expected lowering of apparent integrated intensity for the ν_1 band as the concentration increased. As expected, the amount of absorbance "lost" at a given concentration decreased as the pressure increased, due to pressure broadening of the spectrum. As a result of these calibrations, the observed nitric acid ν_1 integrated absorbances were scaled by correction factors $(1 + f)$ derived as a function of both pressure and observed integrated absorbance.

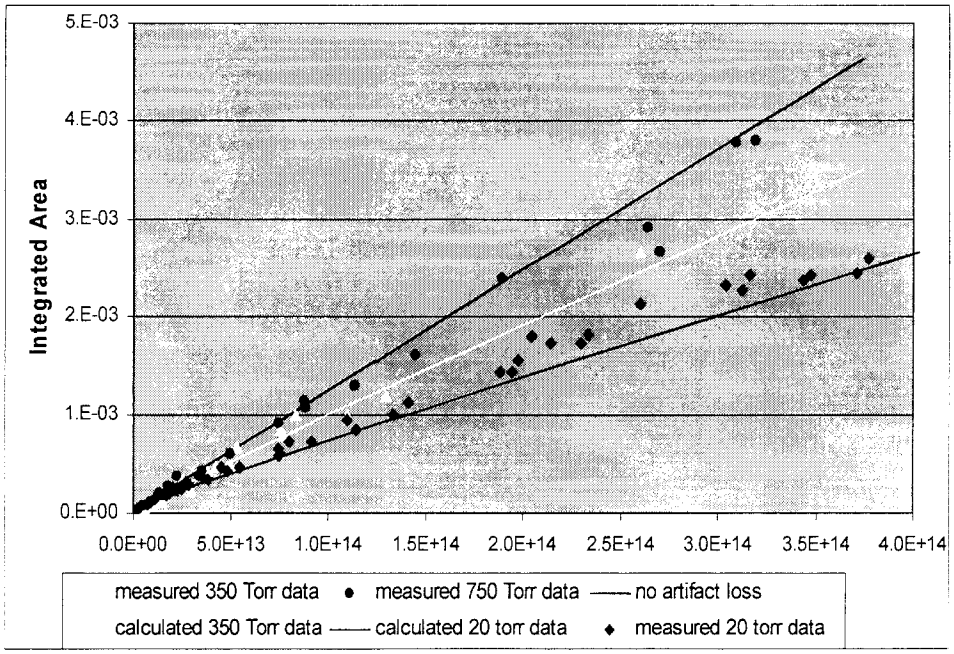

Figure 13 - Calculated and measured calibration data for the $HONO_2$ ν_1 integrated absorbance.

A typical product spectrum of Reaction 1 with H_2 as the source of OH is shown in Figure 14. Features due to $HONO_2$, HOONO and HONO are all clearly present. This same spectrum with the scaled reference spectra used for fitting the observed spectral features is shown in Figure 15. The raw data is shown in black, while the sum of the component spectra is shown in red. A typical product spectrum of Reaction 1 with CH_4 as the OH source is shown in Figure 16. In addition to the features seen in Figure 14, a

formaldehyde band is also present at 3495 cm^{-1}, although its location between the HOONO and $HONO_2$ ν_1 bands does not further complicate the analysis of the spectrum.

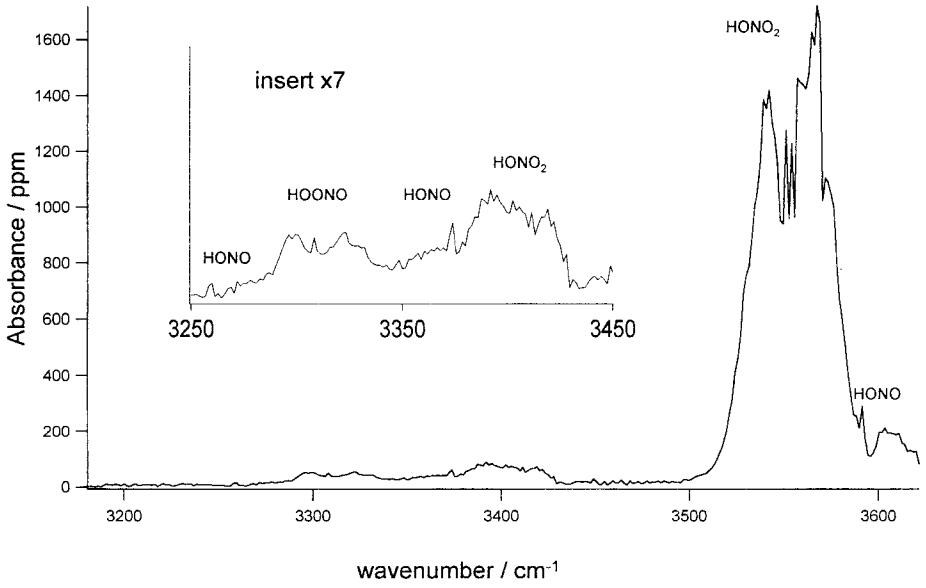

Figure 14 - IR-CRDS spectrum of the products of the reaction OH + NO_2 using $O(^1D)$ + H_2 as the OH source.

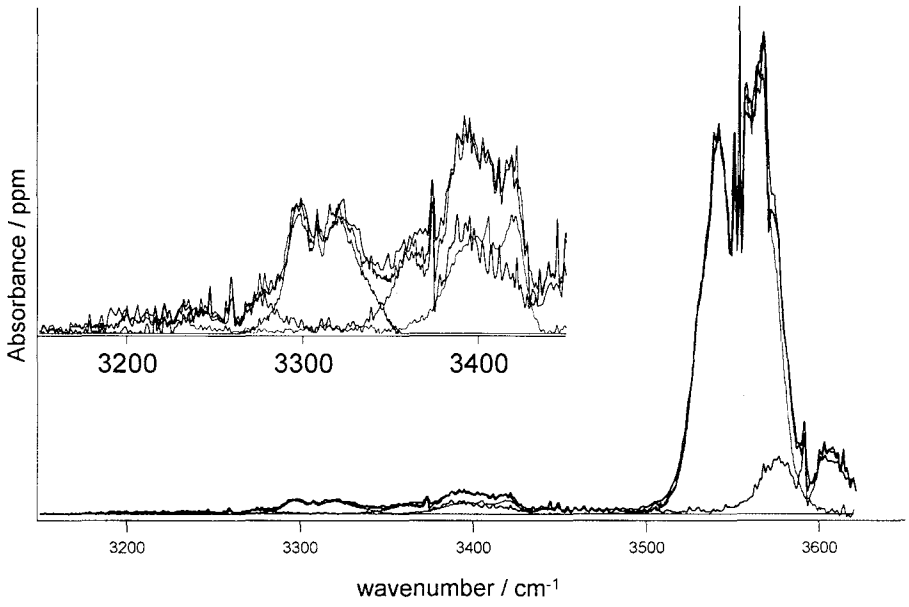

Figure 15 - spectrum shown in previous figure, fit with spectral components due to $HONO_2$ (green), HONO (blue), and HOONO (purple)

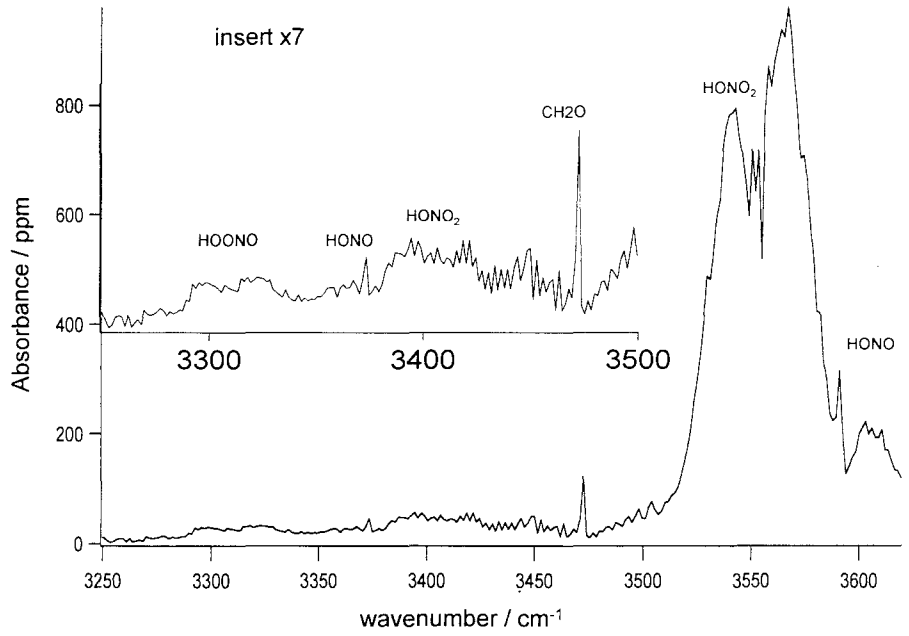

Figure 16 - IR-CRDS spectrum of the products of the reaction OH + NO_2 + M using $O(^1D)$ + CH_4 as the OH source.

All of the HOONO/$HONO_2$ branching ratio measurement data is given in Table 4. This data is plotted in the top portion of Figure 17. The bottom portion of Figure 17 shows the data averaged at each pressure with the 1σ standard deviation of the data shown for each pressure. The conversion from the raw integrated absorbance data shown in Table 4 to the branching ratios shown in Table 4 was done as follows. Nitric acid ν_1 integrated absorbances were multiplied by the scaling factors described above. A $HONO_2$ ringdown correction term *f* accounts for the underestimation of the HONO2 absorbance due to the above-mentioned ringdown effect. The apparent $HONO_2$ integrated absorbance listed in col. 4 was subsequently multiplied by (1+*f*). HOONO integrated absorbances were multiplied by 1.35 to account for absorption which is shifted from the main peak through OH-stretch/torsion coupling and therefore not observable in our spectra(discussed in Task III). The ratio of calculated $HONO_2$/HOONO band intensities of 2.71 was used (discussed in Task III).

Table 4 – Branching ratio data.

OH source indicates reactant with $O(^1D)$. A $HONO_2$ ringdown correction tem of *f* indicates that the $HONO_2$ integrated absorbance listed in column 4 was subsequently multiplied by (1+*f*) when calculating the branching ratio.

		Integrated Absorbance / ppm			
Pressure	OH source	HOONO	$HONO_2$	$HONO_2$ correction term *f*	branching ratio
25	H2	548	31850	0.375	0.046
25	H2	729	35093	0.375	0.055
25	H2	802	33339	0.375	0.064
25	H2	738	33621	0.375	0.058
25	H2	428	22012	0.340	0.053
25	H2	517	22012	0.340	0.064
35	H2	1039	33010	0.375	0.084
35	H2	830	34670	0.375	0.064
50	H2	860	36613	0.360	0.063
50	H2	1148	40342	0.365	0.076
50	H2	1094	39950	0.365	0.073
50	H2	1183	37835	0.365	0.084
50	H2	946	37083	0.360	0.069
57.4	CH4	844	22341	0.330	0.104
70	H2	851	32242	0.341	0.072
71	H2	1683	68730	0.307	0.069
75	H2	1040	42096	0.350	0.067
75	H2	1220	48504	0.350	0.068
75	H2	1039	43835	0.350	0.064
75	H2	1034	34937	0.345	0.081
75	H2	1252	39825	0.350	0.085
80	CH4	1054	31114	0.335	0.093
95	H2	1111	35626	0.330	0.086
100	H2	923	26007	0.315	0.099
100	CH4	1418	44415	0.325	0.088
100	CH4	1144	36503	0.325	0.087
100	CH4	1374	43240	0.325	0.088

100	CH4	824	19019	0.285	0.123
100	H2	1227	40107	0.337	0.084
100	H2	1187	38744	0.335	0.084
100	H2	1184	38665	0.335	0.084
100	H2	1110	36143	0.333	0.084
100	H2	1074	36159	0.333	0.082
100	H2	1118	36409	0.333	0.084
100	H2	1490	48191	0.337	0.085
100	H2	1459	50180	0.337	0.080
100	H2	891	29845	0.322	0.083
100	H2	828	28169	0.322	0.081
100	H2	1037	34655	0.327	0.082
100	H2	940	32414	0.327	0.080
100	H2	1029	42582	0.336	0.066
100	H2	1530	57074	0.338	0.073
100	H2	1107	34185	0.325	0.089
100	H2	645	19192	0.290	0.095
100	H2	1225	41548	0.337	0.081
100	H2	846	28983	0.315	0.081
100	H2	1008	37443	0.335	0.074
100	H2	809	32602	0.325	0.069
100	H2	762	30879	0.325	0.068
100	H2	1121	37522	0.335	0.082
100	H2	1377	46373	0.335	0.081
100	H2	1054	38947	0.335	0.074
100	H2	1258	41642	0.335	0.083
100	H2	1253	39527	0.335	0.087
100	H2	1253	38305	0.335	0.090
102	CH4	1507	43287	0.335	0.095
102	CH4	1507	47689	0.335	0.087
103	H2	744	29375	0.320	0.070
116	CH4	962	25161	0.310	0.107
180	H2	917	28435	0.283	0.092
200	H2	2585	75983	0.240	0.100
200	CH4	1504	46593	0.282	0.092
200	CH4	1582	52327	0.282	0.086
200	CH4	1263	46154	0.282	0.078
200	CH4	1200	38697	0.282	0.089
200	CH4	1205	29955	0.275	0.115
200	H2	1979	63654	0.270	0.090
200	H2	2176	73336	0.250	0.087
200	H2	1639	51324	0.280	0.091
200	H2	1369	39621	0.280	0.099
200	H2	1369	41595	0.280	0.094
200	H2	2146	66662	0.270	0.093
201	CH4	1152	35407	0.282	0.093
201	CH4	1567	46405	0.285	0.096
225	H2	1064	39073	0.275	0.078

230	H2	1645	58985	0.265	0.081
252	H2	1238	32931	0.255	0.110
300	H2	1598	49146	0.250	0.095
305	CH4	1582	46593	0.245	0.100
305	CH4	1739	48598	0.245	0.105
305	CH4	1645	39558	0.235	0.123
350	H2	990	25239	0.200	0.120
350	H2	1286	35360	0.215	0.110
350	CH4	2742	58076	0.225	0.141
350	CH4	2084	57183	0.225	0.109
351	H2	1061	31709	0.215	0.101
357	H2	1777	50823	0.225	0.104
373	H2	2608	77722	0.187	0.103
400	CH4	2256	51105	0.210	0.133
400	CH4	2037	51105	0.210	0.120
400	CH4	1911	45653	0.210	0.127
400	CH4	1485	37631	0.200	0.120
405	H2	417	14279	0.155	0.093
408	H2	1561	36519	0.200	0.130
410	H2	784	28184	0.187	0.086
490	H2	1307	31725	0.157	0.130
500	H2	1974	63090	0.150	0.100
500	H2	4011	94642	0.165	0.133
500	H2	2052	62933	0.150	0.104
500	H2	4105	105734	0.165	0.122
500	H2	3901	95426	0.165	0.128
500	H2	3165	99718	0.165	0.100
500	H2	3807	99718	0.165	0.120
501	CH4	1164	22654	0.140	0.165
505	CH4	2303	48990	0.170	0.147
505	CH4	2193	51042	0.170	0.134
510	H2	1495	43412	0.170	0.108
520	CH4	1280	28545	0.140	0.144
582	H2	1436	33198	0.135	0.139
605	CH4	2146	51449	0.137	0.134
605	CH4	2648	56776	0.137	0.150
606	CH4	1487	34310	0.125	0.141
610	H2	2059	53705	0.137	0.123
614	H2	1401	34059	0.125	0.134
654	H2	1227	30675	0.115	0.131
710	CH4	2256	53799	0.112	0.138
710	CH4	2256	50713	0.112	0.146
710	CH4	2538	51951	0.112	0.161
716	CH4	1318	26868	0.090	0.165
730	H2	1712	44415	0.110	0.127
732	H2	1625	39715	0.100	0.136
750	H2	3859	94705	0.085	0.137
750	H2	3118	76579	0.100	0.135

750	H2	2256	58202	0.105	0.128
750	CH4	3290	76015	0.100	0.144
750	CH4	2491	76015	0.100	0.109
770	H2	2143	51669	0.100	0.138
770	H2	1212	27840	0.085	0.147

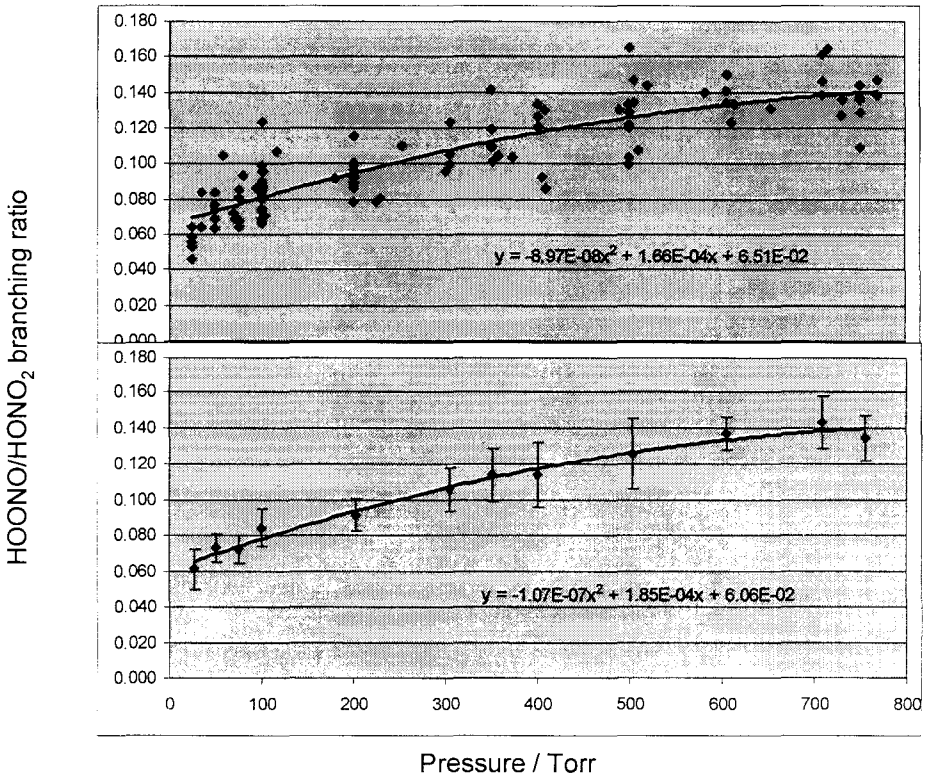

Figure 17 - $HOONO/HONO_2$ Branching ratio data. Upper panel shows all data points and 2nd order polynomial fit to those points. Lower panel shows the same data averaged at each pressure and the fit to those points.

Discussion

The error bars shown in the lower panel of Figure 17 represent the scatter in our data points from one data set to the next. There are three main sources of this scatter. The signal to noise ratio at the peak of the HOONO band was generally low, especially at the highest pressures, where the background noise increased. This led to uncertainty in the fit of the HOONO band. We also observed at times a constant offset between the excimer on and excimer off data, presumably due to slight changes in the alignment of the ringdown cavity due to local heating or photoacoustic effects. This baseline appeared to be constant within a scan, but varied randomly from scan to scan and could be negative or positive. The subtraction of this baseline led to some uncertainty in the derived integrated absorbances, especially for weak bands such as HOONO. There is also some

random uncertainty in the subtraction of the other absorbing species surrounding HOONO, especially the $2\nu_2$ band of trans-HONO which overlaps with the R-branch of HOONO. This uncertainty is fairly small, however, as the P and Q-branches of the HOONO band are free from interference.

Many experiments were performed to investigate potential sources of systematic errors in our branching ratio measurements. The delay time between initiation of the chemistry by photolysis and probing of the products at constant reactant concentrations was varied to investigate the possible influence of HOONO dissociation. The ratio of the concentrations of OH and NO_2 were varied to look for evidence of the potential influence of the reaction OH + HOONO. Evidence of N_2O_4 was observed in our high pressure data, so an experiment was conducted at high pressure which varied the amount of N_2O_4 and look for the potential influence of OH + N_2O_4 on the branching ratio. Lastly, we were concerned about potential influence of vibrationally excited OH produced from $O(^1D) + H_2$ and H + NO_2 on the product branching ratio. As a result, a series of experiments were carried out with $O(^1D)$ + CH_4 as the source of OH. While the OH produced in this manner is not without vibrational excitation, it is much colder than that produce when using H_2. None of the experiments described above showed any variation in the HOONO/$HONO_2$ branching ratio outside the normal scatter in our measurements. As a result, we conclude that while some of these processes may have a small impact on the branching ratio, the uncertainty they introduce is encompassed in the error bars shown in the lower graph of Figure 17.

In addition to the experimental uncertainties discussed above, there are some significant potential systematic errors in our conversion of experimentally measured HOONO and $HONO_2$ integrated absorbances to a product branching ratio. The uncertainty in our correction factors to the $HONO_2$ integrated absorbance, which increase the $HONO_2$ integrated absorbance, is estimated to be 15%. Since the correction factors lead to an increase in the nitric acid integrated absorbance from 10-30%, the uncertainty in the correction factor leads to a 2-5% uncertainty in the calculated branching ratios. The uncertainty in the calculated ratio of cross sections for the two ν_1 bands is estimated to be on the order of 10%. The HOONO integrated absorbance not included in the main peak is 25±5% (see Task 3 for further discussion) leading to a 5% uncertainty in the calculated branching ratio. As a result, when these uncertainties are added in quadrature the overall systematic uncertainty (1σ) is 12%, about the same as the random experimental uncertainty. The branching ratio data has been fit to a second order polynomial in five ways, as shown in Table 5. The only fit which gives significantly different fit parameters comes from fitting the raw data with no systematic uncertainty included in the least squares fitting routine, as is shown in the top portion of Figure 17. All fits which contain either systematic or experimental uncertainty or both give very similar fit parameters, with the only variation in the uncertainty in those fit parameters. The fit of the raw data with each point given the systematic uncertainty (row 2) has been used for calculations of k_{1b} and k_{1a} discussed previously in Task I.

Table 5 – Fit parameters to the branching ratio (k_{1b}/k_{1a}) data as a function of pressure.

Data was fit to the functional form BR = K0 + P*K1 + K2*P^2. 1σ uncertainties in the fit parameters are given. Pressures are in Torr.

	K0	K1	K2
raw data (no uncertainty)	0.0652±0.027	$1.66\pm0.20\times10^{-4}$	$-9.0\pm 2.7\times10^{-8}$
raw data (systematic uncertainty)	0.0608±0.020	$1.79\pm0.18\times10^{-4}$	$-10.8\pm 2.6\times10^{-8}$
averaged data (no uncertainty)	0.0604±0.029	$1.86\pm0.19\times10^{-4}$	$-10.8\pm2.5\times10^{-8}$
averaged data (experimental uncertainty)	0.0606±0.065	$1.87\pm0.55\times10^{-4}$	$-10.9\pm 7.3\times10^{-8}$
averaged data (exp+systematic uncertainty)	0.0604±0.088	$1.87\pm0.75\times10^{-4}$	$-11\pm 10\times10^{-8}$

Task III - Calculation of HOONO and $HONO_2$ Absorption Band Intensities

Objectives

To determine the integrated absorption intensity ratios used in the branching ratio measurements by high level theory, with experimental checks performed to validate the calculations.

Background

The HOONO/$HONO_2$ branching ratios reported in the cavity ringdown experiment (Task 2) are derived from measurements of the absorbance of the observed ν_1 (OH stretch) bands of the relevant species, integrated over the observed band profile. The concentration ratios thus depend upon the ratio of the respective band intensities (integrated cross sections):

$$\frac{n_{\mathrm{HOONO}}}{n_{\mathrm{HONO_2}}} = \frac{I_{\mathrm{HONO_2}}}{I_{\mathrm{HOONO}}} \times \frac{\int A_{\mathrm{HOONO}}(\nu)d\nu}{\int A_{\mathrm{HONO_2}}(\nu)d\nu}$$

While the absolute integrated absorption intensity of the nitric acid ν_1 band has been measured (to within 10%), the HOONO intensity is not known and is not readily measured. The reactions and photodissociation of HOONO have not yet been studied, so titration or photometric methods cannot be used.

In order to derive the branching ratio, we therefore need to rely on theoretical calculations of integrated vibrational intensities. Fortunately, since we are measuring branching *ratios*, only the relative intensities are needed. It is well known that such calculated ratios are more robust, as significant cancellations occur when comparing similar vibrations.

Modern quantum chemical calculations of closed-shell, semi-rigid molecules such as nitric acid can be performed with a high degree of accuracy for electronic energies. The accuracy of the method used here, Coupled Clusters with Singles and Double Excitations with perturbative treatment of Triple Excitations, or CCSD(T), has been well established for electronic structure calculations.

To predict infrared spectroscopic properties, one must use the electronic structure results to compute vibrational frequencies and transition dipole matrix elements. Two approximations are commonly made. The first is the so-called double harmonic approximation. For a normal mode i, the energy levels ε_i and the intensity of the fundamental ($v_i = 0$ to 1) transition are:

$$\varepsilon_i = (n + \tfrac{1}{2})h\nu_i$$

$$I_i = \left\| \frac{1}{2}\left(\frac{\partial \boldsymbol{\mu}}{\partial q_i}\right)_0 \langle 1|q_i|0\rangle \right\|^2$$

This approximation assumes that the vibration behaves as a simple harmonic oscillator, and that the dipole transition moment depends solely on the first derivative of the dipole moment μ with respect to the normal mode coordinate q_i (mechanical and electrical harmonicity). While errors in absolute intensities can be 30-40%, the errors in the ratio are expected to be much less.

A second common assumption is that all molecules absorb within the observed band envelope. At thermal energies, a significant population of molecules are vibrationally excited. If those excited molecules have OH stretch vibrations that absorb infrared radiation at significantly different frequencies (sequence bands), then integration of the observed fundamental band will not include the population of such molecules. Such shifts of the position of sequence bands occurs when there is strong coupling of the observed mode (OH stretch, in this case) with other vibrations.

One must go beyond the simple harmonic oscillator to describe correctly vibrational frequencies and intensities. Normally, one can use perturbation theory to compute corrections to vibrational energies and intensities. Typically, inclusion of cubic and quartic anharmonic force constants allow one to approach near spectroscopic accuracy. Typically, the accuracies are <1% on vibrational frequencies, and 10-20% for absolute intensities, which are generally more difficult to measure). These are complex calculations requiring on the order of 2000 high order force contants coupling the nine degrees of freedom in a pentatomic molecule like HOONO.

Even perturbation theory can lead to significant errors if the amplitude of the vibrations is large and the harmonic oscillator approximation breaks down. *Cis-cis* HOONO has two such modes, the low frequency torsional rotation of the heavy atoms about an ON bond, and that of the OH group about the OO bond (the HOON dihedral angle). The latter HOON dihedral motion may in particular critically affect the OH vibration, because it breaks the weak internal hydrogen bond; this can cause the OH frequency to shift by +250 cm^{-1}, and the intensity to increase by a factor of >2. In this case, one must explicitly map out the potential energy surface and numerically solve the vibrational Hamiltonian. Since a full nine dimensional calculation is not feasible at the highest levels, one must select a subset of the space or degrees of freedom.

Our earlier low pressure branching ratio determination was based on very high level quantum chemistry calculations, the CCSD(T)/AUG-ccpVTZ level, but made the double harmonic approximation. The previous double-harmonic estimate of the intensity ratio was

$$\frac{I_{1,HONO_2}}{I_{1,HOONO}} = 2.71$$

In this approximation, there is no coupling among modes, and hence effectively one assumes that all molecules are detected. The goal of Task III is to improve on our theoretical estimates of the absorption intensity ratio using vibrational perturbation theory, and to compute population corrections for *cis-cis* HOONO by explicitly calculating the effects of OH-stretch/OH-torsion coupling.

Approach

For nitric acid, second order vibrational perturbation theory to compute cubic and quartic anharmonicities is sufficient to obtain frequencies and intensities. However, for *cis-cis* HOONO, one must both perform second order perturbation calculations and treat the torsional motion of the HO group (q_9). and its coupling to the OH stretch mode (q_1).

We have been collaborating with Professor John F. Stanton on calculations of HOONO and related species. He has completed a high level (CCSD(T)/ANO) calculation of the full quartic force field of $HONO_2$ and of all isomers of HOONO within the second order vibrational perturbation theory (VPT2). He has provided results on the intensities of the fundamental IR frequencies and intensities of the ν_1 (OH stretch) vibration. We report his results here.

In a collaboration with Professors Joseph Francisco (Purdue) and Anne McCoy (Ohio State), we have developed a full two-dimensional calculation of the HOONO OH stretching-OH torsion potential energy and dipole moment surfaces.

1) We have computed the relevant portion of the HOONO potential energy and dipole moment surfaces using highly accurate *ab initio* methods (CCSD(T)/cc-pVTZ), coupled with rigorous vibrational calculations to determine vibrational band positions and intensities. We have employed a 2D model, which explicitly treats coupling of the OH stretch and the OH internal rotation (HOON torsion).
2) Using these calculations, we have succeeded in assigning the structure of the OH first overtone spectrum, previous observed by action spectroscopy by Nizkorodov and Wennberg[5]. These results demonstrate that we have quantitatively described the coupling of the OH stretch and torsion modes involved. At least one other mode, which we have neglected, is important.
3) As a further test, we performed cavity ringdown spectroscopy of the overtone spectrum of *cis-cis* HOONO, in the laboratory of Paul Wennberg.

Results and Discussion.

High level quantum chemistry calculations with VPT2

Prof. John F. Stanton, U Texas, with researcher Mychel Varmer have computed properties of HOONO, $HONO_2$, and related species using state-of-the-art methods. At our request, they have computed accurate values of the HOONO and $HONO_2$ ν_1 intensities, taking into account anharmonicities using analytic gradients and second order vibrational perturbation theory (VPT2). These calculations are full nine dimensional expansions of the potential energy and dipole surface about the geometry at the potential minimum, with anharmonic force constants derived to 2^{nd} order PT. They are derived from analytic derivatives at the CCSD(T)/triple-zeta with double polarization.

The results are given in Table 6.

Table 6 – comparison of HOONO frequency and intensity calculations.

		Harmonic	Harmonic	Anharmonic	Experiment
		CCSD(T)/ AUG-cc-pVTZ Francisco	CCSD(T)/ ANO Stanton	CCSD(T)/ ANO Stanton	
HOONO					
	ω_1, cm^{-1}	3521		3320	3306[a]
	$2\omega_1$, cm^{-1}	7042		6415	6350[c]
	I_1, km/mol	33.2	33.4	27.0	
$HONO_2$					
	ω_1, cm^{-1}	3753		3560	3550
	I_1, km/mol	95.4	88.6	73.2	75[b]
	$2\omega_2$, cm^{-1}			3436	3406
	I_{2v2}			2.2	
	$I_{1,HONO2}/I_{1,HOONO}$	2.87	2.65	2.71	

a.Bean et al.[2]
b.Chackerian et al.[46]
c. Fry et al.[33]

There is excellent agreement between Stanton's CCSD(T)/ANO prediction for the ν_1 frequency of cis-cis HOONO (3320 cm^{-1}) using the quartic force-field, and the experimental value (3306 cm^{-1}). Theory similarly predicts the vibrational frequencies of the OH stretch and $2\nu_2$ overtone of $HONO_2$ to a similar degree of accuracy.

The anharmonicity-corrected CCSD(T)/ANO prediction of the infrared intensity of the ν_1 stretch $I_{1,HONO2}$ is 73.2 km/mol, also in good agreement with the most recent experimental value, 75 km/mol, obtained by Chackerian et al.

Based on the CCSD(T)/ANO calculations and VPT2, we have obtained a ratio of the nitric acid to *cis-cis* HOONO infrared intensities of

$$\frac{I_{1,HONO_2}}{I_{1,HOONO}} = 2.71$$

This is very close to the ratio of the intensities computed in the harmonic approximation, 2.86, despite the large discrepancies in the absolute intensities (approximately 30%). This suggests that taking the intensity ratio for like bonds (OH stretch) leads to large cancellations of error.

Calculation of Stretch-Torsion Coupling

Based on our full two-dimensional calculation with Francisco and McCoy, we have predicted the fundamental ν_1 band of *cis-cis* HOONO, taking into account coupling

of the OH stretch with the HOON torsion, ν_9. The details are reported in the attached publication.

As can be seen in the calculated spectrum shown in Figure 18, the origin line near 3300 cm^{-1} dominates the spectrum. This line corresponds to the pure OH stretch transition,with no initial torsional excitation. The absolute position (3270 cm^{-1}) is off by about 30 cm^{-1} (1%), but since this calculation neglects 7 of 9 modes, we do not expect it to reproduce the absolute position exactly. Relative shifts of combination bands with the torsional mode should be fairly accurate. The second dominant band seen in the simulated spectrum, at approximately 3375 cm^{-1}, is the sequence OH stretch band ν_9=1→1, where ν_9 is the torsional vibration quantum number. In other words, this is the OH stretch excitation for excited molecules with one quantum of torsional excitation. The ν_9=2→2 sequence band is also visible, red-shifted to approximately 3430 cm^{-1}. The broad, multiple-band feature around 3600 cm^{-1} comprises a series of $\Delta\nu_9$=1 bands that sample the broad shelf of the torsional potential surfaces, shown in Figure 19. For ease of visualization, we show in this figure the vibrationally adiabatic torsional potential, obtained by averaging the two-dimensional surface over a specific v state in the OH stretch. This adiabatic surface is obtained using the torsional angle dependence of the equilibrium frequency and ahnarmonicity, and adding to the electronic torsional potential energy surface ($U_e(\tau)$):

$$U_v(\tau) = \omega_e(\tau)\left(v + \frac{1}{2}\right) - \omega_e x_e(\tau)\left(v + \frac{1}{2}\right) + U_e(\tau)$$

The transitions mentioned above are shown in Figure 19. This sampling of initially torsionally excited population results in the broad, complex spectrum shown in Figure 18.

The validation of this 2-D model was achieved by comparison of the first OH overtone cavity ringdown absorption spectrum and action spectrum with model predictions. The difference between these two spectra is due to the dissociation threshold for HOONO falling in the first OH overtone region. The resulting quantum yield variation was also modeled. The details of this validation are described in the attached publication. In both cases, this simple 2-D model was shown to reproduce the major features in the spectra. Only one experimentally observed band, suspected to be a combination band with a mode not treated in this model, was not reproduced in the model of the first OH overtone spectrum. This gives us confidence in the same model's predictions for the fundamental band (shown in Figure 18).

The fundamental band at 3306 cm^{-1} detected in the cavity ringdown experiment probes only the ν_9=0 level. Elementary statistical mechanical calculations, as well as inspection of the simulated spectrum (Figure 19), indicate that about 28 ± 5% (1σ) of the population (all molecules with ν_9>0) have OH stretch bands that are displaced to the blue and hence not included in the CRDS integration of the intensity of the band at 3306 cm^{-1}. The error bars of 5% in this case reflect our estimate of the agreement between model and experiment from the OH first overtone (shown in attached publication). As a result of these calculations, the measured HOONO integrated absorbances listed in Table 4 have been multiplied by 1.4 when the branching ratio is calculated.

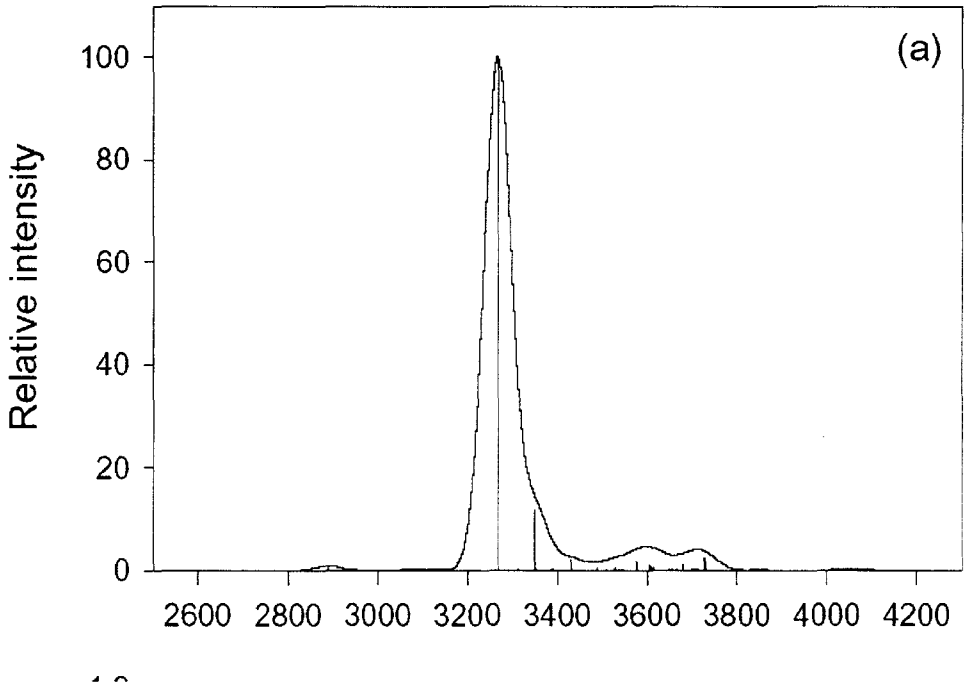

Figure 18. The calculated OH-stretch absorption spectrum of *cis-cis* HOONO predicted using a two-dimensional model incorporating torsion-stretch coupling.

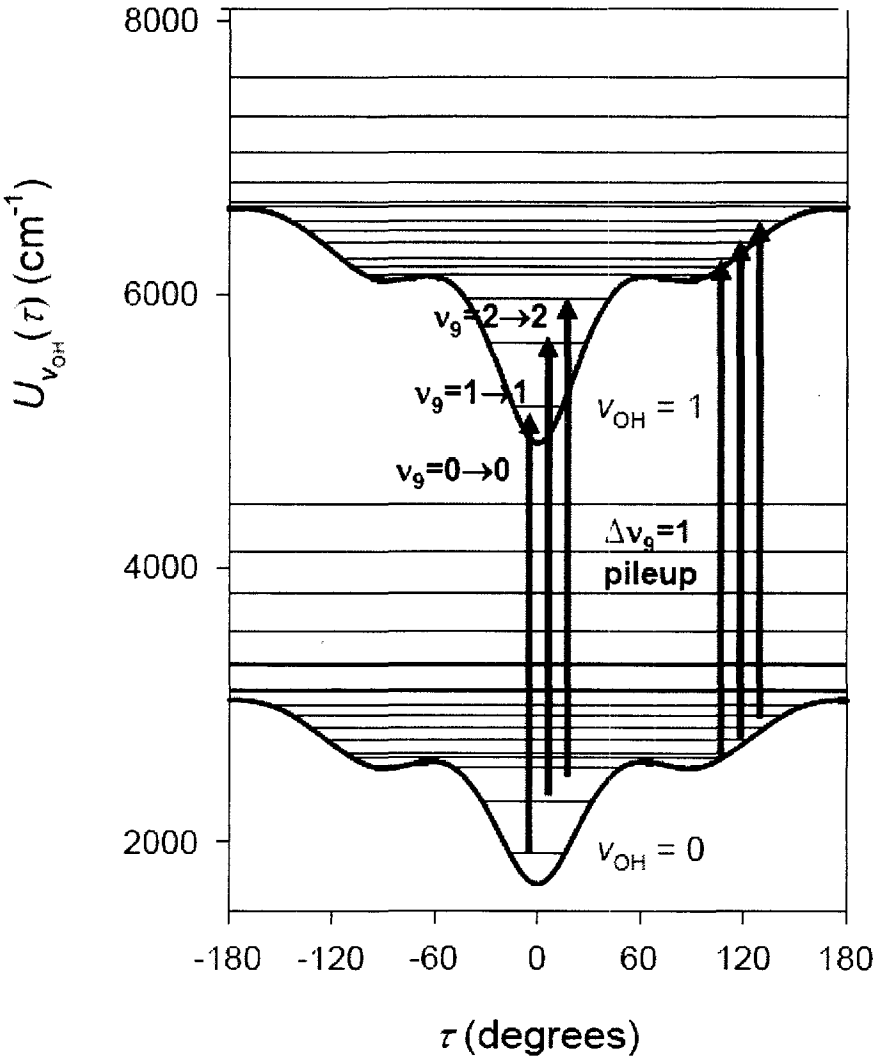

Figure 19 Vibrationally adiabatic potential energy surfaces $U_{v_{OH}}$ for v_{OH}=0 and 1, plotted as a function of τ. The thin lines on each of the adiabatic potential curves represent the energies $E(v_{OH}, n)$ of the torsional states that are associated with the specific v_{OH} quantum level. Sequence band transitions mentioned in the text are shown as vertical arrows (three center transitions).

Discussion and Recommendations

Task I

The rate of reaction 1 has been measured over the range 50-900 Torr. A fit of our k_1 data with M=air to the JPL formulation of the three-body fall-off expression gives

298 K $k_0 = (1.6 \pm 0.1) \times 10^{-30}$ cm^6 molecule^{-2} s^{-1}
$k_\infty = (3.0 \pm 0.3) \times 10^{-11}$ cm^3 molecule^{-1} s^{-1}.

315 K $k_0 = (1.5 \pm 0.1) \times 10^{-30}$ cm^6 molecule^{-2} s^{-1}
$k_\infty = (2.3 \pm 0.3) \times 10^{-11}$ cm^3 molecule^{-1} s^{-1}.

The overall uncertainty in these rate measurements is estimated to be ≈7%.

At 760 Torr and 298 K, we find an effective bimolecular rate of

$k_1 = (1.0 \pm 0.1) \times 10^{-11}$ cm^3 molecule^{-1} s^{-1}.

This value is 14% and 7% lower than the rates derived from the NASA/JPL and IUPAC(2005) recommendations respectively.

Task II

With the aid of the calculations presented in Task III, the HOONO/$HONO_2$ branching ratio has been measured over the range 25-770 Torr at 300 K. A fit of the branching ratio data to a second order polynomial leads to the expression

$$BR = 0.0608 \pm 0.0020 + (1.79 \pm 0.18) \times 10^{-4} P - (1.08 \pm 0.26) \times 10^{-7} P^2$$

where the 1σ uncertainties of the fit parameters are included in parenthesis and P is in Torr. At 750 Torr and 298 K, the measured branching ratio is $k_{1b}/k_{1a} = 0.14 \pm 0.02$.

These branching ratios were measured in a gas mixture consisting of 90% N_2, 9% H_2, and 1% NO_2. Our assumption is that the branching ratio is relatively insensitive to the composition of the gas. There was insufficient time to complete the temperature dependence, but results from previous experiments at low pressure indicate that there is little variation in the branching ratio at an effective pressure of P_{eff}= 13 Torr.

Task III

The $HONO_2$/HOONO relative intensity has been calculated with high level quantum chemistry calculations and second order vibrational perturbation theory. We find the ratio to be 2.71. Additionally, calculations show that 27% of the total HOONO ν_1 band intensity lies outside the main peak due to stretch-torsion coupling and is therefore not observed in the experiments described by *Task II*. These correction factors were incorporated into the analysis of the HOONO and $HONO_2$ spectra to determine the branching ratio given above.

Rate Parameters

From the branching ratio and our experimental data k_1 in M = Air, we derived the fall-off parameter for the separate HOONO and $HONO_2$ channels from

$$k_{1a} = k_1 * \frac{1}{1+BR}$$

$$k_{1b} = k_1 * \frac{BR}{1+BR}$$

Parameters for fits of our data to the NASA/JPL formulation of the three body fall-off expression for 298 K and 315 K are shown in Table 7. Table 8 gives our falloff fit parameters compared with the NASA/JPL recommendation and the master equation results of Golden et al fitted to the NASA/JPL formulation reported in NASA /JPL 2002.

Table 7– Fitted falloff parameters (NASA/JPL formulation, M = air)

	HOONO		HNO_3	
	k_0 cm^6 molecules $^{-2}$ s^{-1}	k_∞ cm^3 molecules $^{-1}$ s^{-1}	k_0 cm^6 molecules $^{-2}$ s^{-1}	k_∞ cm^3 molecules $^{-1}$ s^{-1}
298 K	$(8.6\pm0.4)\times10^{-32}$	$(9.2\pm0.8)\times10^{-12}$	$(1.5\pm0.9)\times10^{-30}$	$(2.5\pm0.2)\times10^{-11}$
315 K	$(7.7\pm0.8)\times10^{-32}$	$(8.7\pm0.3)\times10^{-12}$	$(1.4\pm0.3)\times10^{-30}$	$(1.8\pm0.4)\times10^{-11}$

Table 8 - Comparison of the fitted falloff parameters (NASA/JPL formulation, M = air).

	HOONO		HNO_3	
	$k_0(298)$	$k_\infty(298)$	$k_0(298)$	$k_\infty(298)$
NASA/JPL 2002	1.0×10^{-31}	1.0×10^{-10}	2.0×10^{-30}	2.5×10^{-11}
Golden et al	9.1×10^{-32}	4.2×10^{-11}	1.8×10^{-30}	2.8×10^{-11}
Present work	$(8.6\pm0.4)\times10^{-32}$	$(9.2\pm0.8)\times10^{-12}$	$(1.5\pm0.9)\times10^{-30}$	$(2.5\pm0.2)\times10^{-11}$

Lifetime* of *HOONO at Atmospheric Pressure

In Task II, there was no observed variation in the HOONO/$HONO_2$ branching ratio at 750 Torr over the range of delay times used (1-100 ms). This implies that the lifetime of HOONO with respect to unimolecular decomposition at 750 Torr is longer than 100 ms. Additionally, the unimolecular decay rate k_{-1b} of HOONO at 760 Torr can be calculated from our value of k_{1b} in conjunction with an estimate of equilibrium constant for HOONO formation and decomposition,

$$k_{-1b} = k_{1b} / K_{eq1b}.$$

Assuming a value of $K_{eq1b} = 1.92\text{x}10^{-12}$ cm^3 $molecule^{-1}$,[22] the estimated lifetime of HOONO with respect to decomposition back to OH and NO_2 is on the order of 1 second, consistent with our experimental lower limit. This lifetime has two implications:

- The lifetime of HOONO is significantly longer than the timescale of the reactions observed in the experiments described in Task 1. There, OH pseudo-first order decay times were on the order of 10 ms or less, and any HOONO formed by channel 1b would not have redissociated back to OH. Thus, the rate constants

reported are indeed a measure of k_1, the total loss through both channels 1a and 1b.

- In the atmosphere, HOONO decay back to OH and NO_2 by collisional dissociation, $k_{-1b}[M]$, will dominate over other loss processes. The lifetime to photolysis should be on the order of minutes to hours, and the lifetime with respect to reaction with OH should be on the order of 10^4 seconds, even assuming upper limit values of $k = 10^{-10}$ cm^3 molecule^{-1} s^{-1} and [OH] = 10^7 molecules cm^{-3}. As a result, HOONO is a very short-lived transient, and channel 1b is not a net sink for OH and NO_2.

Modeling Recommendations

We recommend that our results can be incorporated into urban airshed models in one of two ways.

(1) COMPLETE MECHANISM

The full reaction scheme, including both reaction 1a and 1b can be used:

$$\begin{aligned} OH + NO_2 + M &\rightarrow HONO_2 & k_{1a} \\ &\rightarrow HOONO & k_{1b} \\ HOONO + M &\rightarrow OH + NO_2 & k_{-1b} \end{aligned}$$

In this case, the rate of collisional dissociation of HOONO back to OH and NO_2, reaction (−1b) must also be incorporated into the models. The parameters to be used in Eq. 1 are

Reaction 1a - $k_{0,1a}$ (298 K) = $(1.5 \pm 0.1) \times 10^{-30}$ cm^6 molecules^{-2} s^{-1}
$k_{\infty,1a}$ (298 K) = $(2.5 \pm 0.2) \times 10^{-11}$ cm^3 molecules^{-1} s^{-1}

$k_{0,1a}$ (315 K) = $(1.4 \pm 0.3) \times 10^{-30}$ cm^6 molecules^{-2} s^{-1}
$k_{\infty,1a}$ (315 K) = $(1.8 \pm 0.4) \times 10^{-11}$ cm^3 molecules^{-1} s^{-1}

Reaction 1b - $k_{0,1b}$ (298 K) = $(8.6 \pm 0.4) \times 10^{-32}$ cm^6 molecules^{-2} s^{-1}
$k_{\infty,1b}$ (298 K) = $(9.2 \pm 0.8) \times 10^{-12}$ cm^3 molecules^{-1} s^{-1}

$k_{0,1b}$ (298 K) = $(7.7 \pm 0.8) \times 10^{-32}$ cm^6 molecules^{-2} s^{-1}
$k_{\infty,1b}$ (298 K) = $(8.7 \pm 0.3) \times 10^{-12}$ cm^3 molecules^{-1} s^{-1}

These rates must be used together with the rate for collisional dissociation of HOONO,

k_{-1b} (298 K, 1atm) = 6.6×10^{-1} s^{-1}

(2) Due to the rapid decomposition of HOONO back to OH and NO_2 under typical urban conditions, our reported value of k_{1a} can be used as an effective loss rate of OH and NO_2 to form the sink $HONO_2$. We therefore recommend that the values to be used in models be

Reaction 1 - $k_{0,1a}(298\ K) = (1.5 \pm 0.1) \times 10^{-30}\ cm^6\ molecules^{-2}\ s^{-1}$
$k_{\infty,1a}(298\ K) = (2.5 \pm 0.2) \times 10^{-11}\ cm^3\ molecules^{-1}\ s^{-1}$

$k_{0,1a}(315\ K) = (1.4 \pm 0.3) \times 10^{-30}\ cm^6\ molecules^{-2}\ s^{-1}$
$k_{\infty,1a}(315\ K) = (1.8 \pm 0.4) \times 10^{-11}\ cm^3\ molecules^{-1}\ s^{-1}$

For temperatures between 298 K and 315 K a linear interpolation between these values should be used. It should be noted that this study covers a fairly narrow range of temperatures and pressures which are relevant to the lower atmosphere can not be generally extrapolated to all conditions.

Publications

McCoy A.B., Fry, J.L., et al, *Role of OH-stretch/torsion Coupling and Quantum Yield Effects in the First OH Overtone Spectrum of cis-cis HOONO.* J. Chem. Phys., 2005. **122**: 104311.

Glossary

branching ratio	ratio of the rates of two product channels of a reaction. In this case k_{1b}/k_{1a}
CRDS	cavity ringdown spectroscopy
HNO_3	nitric acid
$HONO_2$	nitric acid
HOONO	peroxynitrous acid
IR	infrared
k_1	the effective bimolecular rate constant for the reaction $OH + NO_2 + M \rightarrow$ products
k_{1a}	the effective bimolecular rate constant for the reaction $OH + NO_2 + M \rightarrow HONO_2 + M$
k_{1b}	the effective bimolecular rate constant for the reaction $OH + NO_2 + M \rightarrow HOONO + M$
NO_2	nitrogen dioxide
NO	nitric oxide
NO_x	oxides of nitrogen
O_2	molecular oxygen
O_3	ozone
OH	hydroxyl radical
PLP-LIF	Pulsed Laser Photolysis, Laser Induced fluorescence
$1+f$	Correction factor for absorbance measurements by CRDS

References

1. Russell, A. and R. Dennis, *NARSTO critical review of photochemical models and modeling.* Atm. Environ., 2000. **34**(12-14): p. 2283-2324.
2. Bean, B.D., et al., *Cavity Ringdown Spectroscopy of cis-cis HOONO and the HOONO/HONO2 Branching ratio in the Reaction OH + NO2 + M.* J. Phys. Chem. A, 2003. **107**: p. 6974-6985.
3. Donahue, N.M., et al., *Constraining the Mechanism of OH + NO2 using isotopically labeled reactants: Experimental evidence for HOONO formation.* Journal of Physical Chemistry A, 2001. **105**(9): p. 1515-1520.
4. Hippler, H., S. Nasterlack, and F. Striebel, *Reaction of OH + NO2 + M: Kinetic evidence of isomer formation.* Physical Chemistry Chemical Physics, 2002. **4**(13): p. 2959-2964.
5. Nizkorodov, S.A. and P.O. Wennberg, *First Spectroscopic Observation of Gas-Phase HOONO.* Journal of Physical Chemistry A, 2002. **106**(6): p. 855-859.
6. Anderson, J.G., J.J. Margitan, and F. Kaufman, *Gas phase recombination of hydroxyl radical with nitric oxide and with nitrogen dioxides.* J. Chem. Phys., 1974. **60**(8): p. 3310-17.
7. Erler, K., et al., *The recombination reaction between hydroxyl radicals and nitrogen dioxide. OH + NO2 + M (= helium, carbon dioxide) in the temperature range 213-300 K.* Ber. Bunsenges. Phys. Chem., 1977. **81**(1): p. 22-6.
8. Harris, G.W. and R.P. Wayne, *Reaction of hydroxy radicals with NO, NO2, and SO2.* J. Chem. Soc. Faraday Trans. I, 1975. **71**: p. 610-617.
9. Howard, C.J. and K.M. Evenson, *Laser magnetic resonance study of the gas phase reactions of hydroxyl with carbon monoxide, nitrogen monoxide, and nitrogen dioxide.* J. Chem. Phys., 1974. **61**(5): p. 1943-52.
10. Anastasi, C., P.P. Bemand, and I.W.M. Smith, *Rate constants for hydroxyl + nitrogen dioxide (+ molecular nitrogen) → nitric acid (+ molecular nitrogen) between 220 and 358 K.* Chem. Phys. Lett., 1976. **37**(2): p. 370-2.
11. Atkinson, R., R.A. Perry, and J.N. Pitts, Jr., *Rate constants for the reactions of the hydroxyl radical with nitrogen dioxide (M = argon and molecular nitrogen) and sulfur dioxide (M = argon).* J. Chem. Phys., 1976. **65**(1): p. 306-10.
12. Atkinson, R., R.A. Perry, and J.N. Pitts, Jr., *Rate Constants for Reaction of OH Radical with CH3SH and CH3NH2 over Temperature Range 299-426 K.* J. Chem. Phys., 1977. **66**: p. 1578.
13. Brown, S.S., R.K. Talukdar, and A.R. Ravishankara, *Rate constants for the reaction OH+NO2+M → HNO3+M under atmospheric conditions.* Chemical Physics Letters, 1999. **299**(3,4): p. 277-284.
14. Donahue, N.M., et al., *High-pressure flow study of the reactions OH + NOx → HONOx: Errors in the falloff region.* Journal of Geophysical Research, [Atmospheres], 1997. **102**(D5): p. 6159-6168.
15. D'Ottone, L., et al., *A pulsed laser photolysis-pulsed laser induced fluorescence study of the kinetics of the gas-phase reaction of OH with NO2.* Journal of Physical Chemistry A, 2001. **105**(46): p. 10538-10543.
16. Dransfield, T.J., et al., *Temperature and pressure dependent kinetics of the gas-phase reaction of the hydroxyl radical with nitrogen dioxide.* Geophysical Research Letters, 1999. **26**(6): p. 687-690.
17. Forster, R., et al., *High pressure range of the addition of HO to HO, NO, NO2, and CO. I. Saturated laser induced fluorescence measurements at 298 K.* J. Chem. Phys., 1995. **103**(8): p. 2949-58.

18. Fulle, D., et al., *Temperature and pressure dependence of the addition reactions of HO to NO and to NO2. IV. Saturated laser-induced fluorescence measurements up to 1400 bar.* Journal of Chemical Physics, 1998. **108**(13): p. 5391-5397.
19. Morley, C. and I.W.M. Smith, *Rate Measurements of Reactions of OH by Resonance Absorption.* J. Chem. Soc. Faraday II, 1972. **68**: p. 1016-1030.
20. Robertshaw, J.S. and I.W.M. Smith, *Kinetics of the hydroxyl + nitrogen dioxide + argon and hydroxyl + nitrogen dioxide + tetrafluoromethane reactions at high total pressures.* J. Phys. Chem., 1982. **86**(5): p. 785-90.
21. Wine, P.H., N.M. Kreutter, and A.R. Ravishankara, *Flash Photolysis-Resonance Flluorescence Kinetics Study of the reaction OH + NO_2 + M → HNO_3 + M.* J. Phys. Chem., 1979. **83**: p. 3191-3195.
22. Sander, S.P., et al., *Chemical Kinetics and Photochemical Data for Use in Atmospheric Studies, Evaluation Number 14.* 2002, Jet Propulsion Laboratory: Pasadena.
23. Atkinson, R., et al., *Evaluated kinetic, photochemical, and heterogeneous data for atmospheric chemistry: Supplement V, IUPAC subcommittee on gas kinetic data evaluation for atmospheric chemistry.* J. Phys. Chem. Ref. Data, 1997. **26**: p. 521-1011.
24. Gilbert, R.G., K. Luther, and J. Troe, *Theory of Thermal Unimolecular Reactions in the Fall-off Range. 2. Weak Collision Rate Constants.* Ber. Bunsenges. Phys. Chem., 1983. **87**: p. 169.
25. Troe, J., *Predictive possibilities of unimolecular rate theory.* J. Phys. Chem., 1979. **83**(1): p. 114-26.
26. Troe, J., *Theory of Thermal Unimolecular Reactions in the Fall-off Range. 1. Strong Collision Rate Constants.* Ber. Bunsenges. Phys. Chem., 1983. **87**: p. 161.
27. Golden, D.M. and J.P. Smith, *Reaction of OH + NO2 + M: A New View.* J. Phys. Chem. A, 2000. **104**: p. 3991-3997.
28. Matheu, D.M. and W.H. Green, Jr., *A priori falloff analysis for OH + NO2.* International Journal of Chemical Kinetics, 2000. **32**(4): p. 245-262.
29. Troe, J., *Analysis of the Temperature and Pressure Dependence of the Reaction HO+NO2+M,<-> HONO2+M.* Int. J. Chem. Kinet., 2001. **33**(12): p. 878-889.
30. Vandaele, A.C., et al., *Fourier Transform Measurement of NO_2 Absorption Cross-sections in the Visible Range at Room Temperature.* J. Atm. Chem, 1996. **25**: p. 289-305.
31. Donahue, N.M., et al., *High - pressure flow study of the reactions OH + NO_x → $HONO_x$: Errors in the falloff region*, in *J. Geophys. Res.* 1997. p. 6159-6168.
32. Anastasi, C. and I.W.M. Smith, *Rate measurements of reactions of hydroxyl by resonance absorption. Part 5. Rate constants for OH + NO2 (+M)→ HNO3 (+M) over a wide range of temperature and pressure.* J. Chem. Soc., Faraday Trans. 2, 1976. **72**(8): p. 1459-68.
33. Fry, J.L., S.A. Nizkorodov, and M. Okumura, *cis-cis and trans-perp HOONO: Action spectroscopy and isomerization kinetics.* J . Chem . Phys . 2004. **121**(3): p. 1432-1448.
34. Zalicki, P. and R.N. Zare, *Cavity ring-down spectroscopy for quantitative absorption measurements.* J. Chem. Phys., 1995. **102**(7): p. 2708-17.
35. Yalin, A.P. and R.N. Zare, *Effect of laser lineshape on the quantitative analysis of cavity ring-down signals.* Laser Physics, 2002. **12**(8): p. 1065-1072.
36. Hodges, J.T., J.P. Looney, and R.D. van Zee, *Laser bandwidth effects in quantitative cavity ring-down spectroscopy.* Applied Optics, 1996. **35**(21): p. 4112-4116.
37. Butler, J., et al., *Vibrational-Excitation of OH(X2-PI) Produced in the the Reaction of O(D-1) with H2.* Chemical Physics Letters, 1983. **95**(3): p. 183-188.
38. Brown, S.S., R.W. Wilson, and A.R. Ravishankara, *Absolute intensities for third and fourth overtone absorptions in HNO3 and H2O2 measured by cavity ring down spectroscopy.* J. Phys. Chem., 2000. **104**(21): p. 4976-4983.

39. Berden, G., R. Peeters, and G. Meijer, *Cavity ring-down spectroscopy: Experimental schemes and applications.* Int. Rev. Phys. Chem., 2000. **19**(4): p. 565-607.
40. Meijer, G., et al., *Coherent cavity ring down spectroscopy.* Chem. Phys. Lett., 1994. **217**(1-2): p. 112-16.
41. Reid, S.A. and Y. Tang, *Generation of tunable, narrow-band mid-infrared radiation through a 532-nm-pumped KTP optical parametric amplifier.* App. Optics, 1996. **35**(9): p. 1473-7.
42. Press, W.H., et al., *Numerical Recipes in Fortran (Second Edition).* 1992, Cambridge: Cambridge University Press.
43. Zalicki, P. and R.N. Zare, *Cavity ring-down spectroscopy for quantitative absorption measurements.* J. Chem. Phys., 1995. **102**(7): p. 2708-2717.
44. Romanini, D. and K.K. Lehmann, *Ring-down cavity absorption spectroscopy of the very weak hydrogen cyanide overtone bands with six, seven, and eight stretching quanta.* J. Chem. Phys., 1993. **99**(9): p. 6287-301.
45. O' Keefe, A. and D.A.G. Deacon, *Cavity ring-down optical spectrometer for absorption measurements using pulsed laser sources.* Rev. Sci. Inst., 1988. **59**(12): p. 2544-2551.
46. Chackerian, C.J., S.W. Sharpe, and T.A. Blake, *Anhydrous Nitric Acid Integrated Absorption Cross Sections: 820 to 5300 cm-1.* J. Quant. Spectros. Radiat. Transfer, 2003.